JOURNAL OF GEOPHYSICAL RESEARCH, VOL. 114, E03004, doi:10.1029/2008JE003163, 2009

Crater-associated dark diffuse features on Venus: Properties of surficial deposits and their evolution

N. V. Bondarenko[1,2] and J. W. Head[2]

Received 11 April 2008; revised 13 December 2008; accepted 31 December 2008; published 12 March 2009.

[1] In order to assess the nature of crater-associated radar-dark diffuse features (DDFs) on Venus and to understand their formation and evolution, we analyzed Magellan radar roughness, emissivity, and reflectivity data in the vicinity of craters accompanied by these features. Following others, we assumed that DDFs are deposits (mantles) of ejected material emplaced during formation of the impact crater. The majority of radar-dark parabolas (the youngest DDFs) are characterized by a smooth mantle-atmosphere interface having low root-mean-square (rms) slopes on scales of 1–100 m, as derived from Magellan altimeter data. Older DDFs also often have areas with low rms slopes, suggesting that the mantle rms slopes can be preserved for geologically long periods of time. Some parabolas and older DDFs have asymmetric small-scale (decimeter-scale) relief that is interpreted to be dunes that formed as a result of eolian processes. This implies that the mantle material is mobile and can saltate under the influence of wind action. On average, aging of these features is accompanied by a decrease of mantle material dielectric permittivity. The most efficient mechanism for parabola degradation seems to be the removal of mantle material from the site of initial deposition by subsequent winds. We found a few examples of features that could be interpreted to be the result of in situ modification of the primary mantle.

Citation: Bondarenko, N. V., and J. W. Head (2009), Crater-associated dark diffuse features on Venus: Properties of surficial deposits and their evolution, *J. Geophys. Res.*, *114*, E03004, doi:10.1029/2008JE003163.

1. Introduction

[2] The population of craters on Venus's surface is rather small, ~1000, primarily because the surface is geologically young, but also because the dense atmosphere causes breakup and filtering of smaller projectiles [*Phillips et al.*, 1992; *Shaber et al.*, 1992]. About 67% of craters with a diameter >5 km [*Basilevsky et al.*, 2003] (see Table 1) are accompanied by radar-dark diffuse features (DDF) seen in synthetic aperture radar (SAR) images. Other published inventories of DDFs and emissivity parabolas [*Campbell et al.*, 1992; *Herrick and Phillips*, 1994; *Basilevsky and Head*, 2002a] are also shown in Table 1. DDFs were interpreted as surficial deposits of loose material up to a few meters thick [*Campbell et al.*, 1992; *Schaller and Melosh*, 1998; *Bondarenko and Head*, 2004]. There are also some diffuse radar-dark deposits associated with volcanic features [*Keddie and Head*, 1995; *Campbell*, 1994]; they could be formed by eruption of volcanic ash or emplacement of loose volcanic deposits formed during eruptions, but the high atmospheric pressure should inhibit gas exsolution and explosive eruptions except under unusual conditions [e.g., *Head and Wilson*, 1992]. The majority of DDFs are related to impact craters and are caused by deposition of mantles composed of ejected material emplaced during impact crater formation on Venus [e.g., *Campbell et al.*, 1992; *Arvidson et al.*, 1992; *Schultz*, 1992].

[3] Shapes and sizes of DDFs vary over a rather wide range. About 10% of the entire crater population on Venus exhibits well-expressed DDFs with parabolic shapes, dubbed dark parabolas (DP) [*Campbell et al.*, 1992] (see Table 1). Such shapes have been explained by transport of material lifted by the westward superrotation of the atmosphere of Venus [*Vervack and Melosh*, 1992; *Campbell et al.*, 1992]. Craters with the DPs are thought to be the youngest on the planet [*Arvidson et al.*, 1992; *Campbell et al.*, 1992]. Other types of DDFs are observed for about half of the craters >30 km in diameter. These include (1) pronounced continuous dark halos around craters, and (2) small radar-dark areas near craters, comprising about 29.4% and 21.4% of the craters, respectively [*Basilevsky and Head*, 2002a] (see Table 1).

[4] DDFs cover large areas, up to ~2,630,000 km^2 for the crater Greenaway dark parabola (DP length is ~1750 km and width is ~1990 km) [*Campbell et al.*, 1992]. In general, the lengths of observed dark parabolas vary from ~11 crater diameters (crater Audrey) up to ~50 crater diameters (crater Ruth) [*Campbell et al.*, 1992].

[5] Some of the observed variability of DDFs can be due to the specific amount of material emplaced and the interplay between the physical properties of the mantle material and the properties and structure of the substrate.

[1]Institute of Radiophysics and Electronics, National Academy of Sciences of Ukraine, Kharkov, Ukraine.
[2]Department of Geological Sciences, Brown University, Providence, Rhode Island, USA.

0148-0227/09/2008JE003163$09.00

Table 1. Summary of Numbers of Craters Associated With Different Types of Radar-Dark Diffuse Features and Emissivity Parabolas[a]

D (km)	N	T	N_T	P (%)
8–105	711[b]	DP	49	6.9
		DH	9	1.3
6–20	509[b]	EP	8	1.6
all	796[c]	DP	87	10.9
		DH	311	39.1
≥22.6	249[d]	DP	20	8.1
		DH	90	36.0
≥30	186[e]	DP	26	14.0
		DH	56	30.1
		FH	40	21.5
≥5	753[f]	DP	51	6.8
		DH	223	29.6
		FH	224	29.7
2.8–92.3	825[g]	EP	44	5.3

[a]DP, radar-dark parabolas; DH, radar-dark halo; FH, faint radar halo; EP, emissivity parabolas; *D,* crater diameters; *N,* number of all craters in corresponding diameters range; *T* and N_T, type of specific appearance of extended crater deposits and corresponding number of craters of this type; *P,* proportion of total number of craters in this category.
[b]*Campbell et al.* [1992].
[c]*Izenberg et al.* [1994], lowlands only (<6053 km).
[d]*Herrick and Phillips* [1994].
[e]*Basilevsky and Head* [2002a].
[f]*Basilevsky et al.* [2003], superposed on wrinkle-ridged regional plains and on the younger units.
[g]*Bondarenko and Head* [2004], in the 66°S–66°N latitude zone.

[6] DDFs shapes and sizes can also be influenced by continued weathering and degradation processes subsequent to their formation. The range of appearance and morphologies of DDFs (from parabolas to halos to one or several faint radar-dark patches) has been interpreted as a DDF degradation sequence ranging from young to old [*Izenberg et al.*, 1994]. Clear examples of craters illustrating such a sequence are shown in Figure 1. DP denotes craters with extended radar-dark deposits of parabolic shape. CH means craters with clear nonparabolic radar-dark halos, FH denotes craters with patchy dark areas (''faint'' nonparabolic halos), and NH denotes craters with no visible dark material nearby. Craters with DDFs have been widely used as control points for estimates of relative ages of geological features and absolute ages of units and features in stratigraphic sequences [*Izenberg et al.*, 1994; *Basilevsky and Head*, 2002b; *Basilevsky and Head*, 2006].

[7] Specific mechanisms of parabola degradation are not well understood. There are several possible scenarios for changing the appearance of DDFs. One scenario is alteration of the mantle through the in situ change of physical, chemical and/or structural properties of the mantle material due to chemical weathering processes [e.g., *Wood*, 1997], which ultimately removes the visible signature of the radar-dark parabola. The existence of altered indurated mantles on Venus is partly supported by the results of the study of Venus surface made by Venera and Vega landers [*Florensky et al.*, 1977; *Basilevsky et al.*, 1985]. Some in situ measurements showed surface material density of ~1.5 g cm^{-3} [*Avduevsky et al.*, 1983], which corresponds to basaltic material with ~50–60% porosity. Spacecraft landing dynamics on Venus point to a rather soft ground, consistent with material ranging from heavily weathered basaltic lavas to mechanically weak volcanic tuff [*Kemurdzhian et al.*, 1983]. The surface material seen in Venus panoramas at the Venera 9, 10, 13, and 14 landing sites has also been interpreted as lithified air fall deposits [*Basilevsky et al.*, 2004], as well as layered rocks [*Florensky*

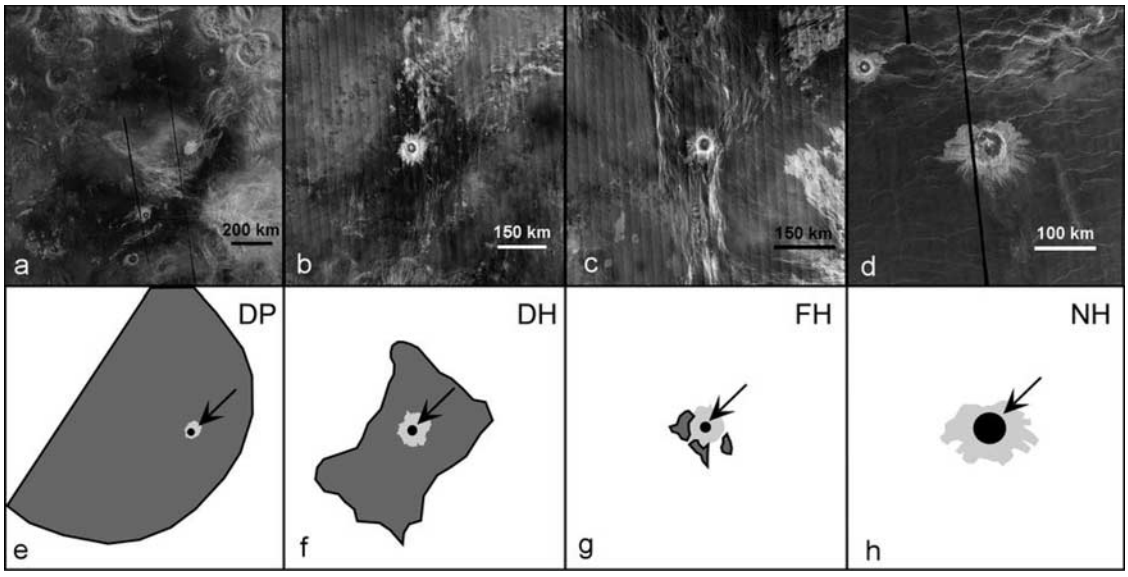

Figure 1. Craters with different types of associated radar-dark features arranged in order of increasing age: (a) dark parabola (DP) crater Sabin (38.5°S, 274.7°E, D = 33.1 km); (b) clear dark halo (DH) crater Hwangcini (6.3°N, 141.8°E, D = 30.2 km); (c) faint dark halo (FH) crater Blackburne (11.0°N, 183.9°E, D = 30.1 km); (d) no halo (NH) crater Barto (45.3°N, 146.2°E, D = 47.9 km); (e) sketch of the dark deposits near the crater Sabin (Figure 1a); (f) sketch of the dark deposits near the crater Hwangcini (Figure 1b); (g) sketch of the dark deposits near the crater Blackburne (Figure 1c); (h) sketch of the crater Barto (Figure 1d). Legend: black circles are crater; light gray is continuous bright deposits; dark gray is radar-dark diffuse features (DDF); arrows show crater location; D is crater diameter.

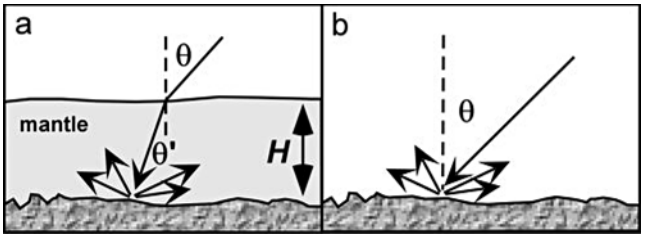

Figure 2. Sketches illustrating the model for microwave properties of (a) mantled and (b) pure surfaces. Incidence angle of radiation is θ, the reflectance angle of radiation inside the mantle is θ', H is mantle thickness. Upper mantle surface is smooth at wavelength scale.

et al., 1977; *Basilevsky et al.*, 1985] and lava flow structure [e.g., *Garvin et al.*, 1984].

[8] Another possible scenario for radar-dark parabola modification and disappearance is eolian activity, the migration and removal of parabola material from the area of initial emplacement due to winds. On the basis of a number of wind-related features seen in Magellan SAR images, eolian processes are known to be rather active on the surface of Venus [*Arvidson et al.*, 1992; *Greeley et al.*, 1997]. There are many wind streaks and numerous examples of the accumulation of dark material in topographic wind shadows [*Greeley et al.*, 1995], two large dune fields, and several areas interpreted to be covered by microdunes [*Weitz et al.*, 1994]. Eolian redistribution of DDF material is widely mentioned as one of the major mechanisms of DDF degradation [*Arvidson et al.*, 1992; *Izenberg et al.*, 1994; *Herrick et al.*, 1997].

[9] In the present work we analyze the life cycle of radar-dark parabolas through these two end-member scenarios of aging processes. We study DDFs using several Magellan data sets including SAR images, ARCDR (Altimeter and Radiometry Composite Data Record), GXDR (Global Topography, Emissivity, Reflectivity, and Slope Data Record) and SCVDR (Surface Characteristics Vector Data Record) (available from the Planetary Data System (PDS) at http://pds-geosciences.wustl.edu/missions/magellan/index.htm) data sets in order to understand the relative role of these mechanisms. In particular, large-scale surface slopes derived from altimeter measurements allow us to look for differences in decameter-scale roughness for mantles of different ages. Fresnel reflectivity and emissivity data serve as a source for estimates of the mantle dielectric permittivity.

[10] We studied in detail the surfaces surrounding young craters to define the specific properties of dark parabolas. We carried out a survey of the vicinities of older craters to find any features that could be interpreted as "altered" or "brightened" parabolas. We also analyzed evidence for reworking of dark parabola material by winds using anisotropy of radar backscattering. The anisotropy was studied using both SAR images and a Doppler centroid map derived from the SCVDR data set.

2. A Model for the Radar Echo of the Mantled Surface and Aging Processes

2.1. Model Description

[11] The change of observed radar brightness of DDFs with age was studied with a simple model of surface structure as a half-space of material with dielectric permittivity ε_S representing the substrate covered by the mantle with dielectric permittivity ε_M and thickness H (Figure 2a).

[12] Radar backscattering from the mantled surface is controlled by several factors. First, the radiation is partly reflected/scattered at the upper interface and partly transmitted into the mantle. Inside the mantle, the radiation is absorbed by mantle material while traveling from the upper interface to the substrate and back. Also the radiation is scattered at the mantle-substrate interface.

[13] In general, the above description can be turned into the expression for the observed radar cross section (hereafter we use the term "radar cross section" meaning "specific radar cross section" throughout the paper):

$$\sigma(\theta) = S(\varepsilon_M, \xi_M, \theta) + F(\varepsilon_M, \tan\delta, \xi_M, \varepsilon_{SM}, \xi_S, \theta), \quad (1)$$

where $S(\ldots)$ is the scattering coefficient at the mantle-atmosphere interface and $F(\ldots)$ is the part of radar echo formed below this interface ("internal" part). ξ_M is the roughness of the upper mantle surface, and θ is the incidence angle of radiation. The state of the mantle-atmosphere interface strongly influences the observed properties of the mantled surface. A very rough mantle-atmosphere interface can be responsible for the major part of the total radar cross section and the substrate thus becomes purely invisible, $F(\ldots) \ll S(\ldots)$. If mantle is smooth at the wavelength scale, then $\xi_M \approx 0$ and $S(\varepsilon_M, 0, \theta) \approx 0$.

[14] If the mantle is homogeneous, the volume scattering may be neglected and the internal part of the radar echo can be written as

$$F(\varepsilon_M, \tan\delta, \xi_M, \varepsilon_{SM}, \xi_S, \theta) = T(\varepsilon_M, \xi_M, \theta) \cdot A(\varepsilon_M, \theta', \tan\delta, H) \cdot U(\varepsilon_S/\varepsilon_M, \xi_S, \theta'). \quad (2)$$

$T(\ldots)$ here is the transmission factor at the mantle-atmosphere interface. If this interface is flat, the transmission coefficient can be written as

$$T(\varepsilon_M, 0, \theta) = \left[1 - R(\varepsilon_M, \theta)^2\right] \cdot \left[1 - R(1/\varepsilon_M, \theta')^2\right], \quad (3)$$

where $R(\varepsilon,\theta)$ is the Fresnel reflection coefficient and θ' is the transmission angle of radiation inside the mantle related to the incidence angle θ at the mantle-atmosphere interface by Snell's law [e.g., *Stratton*, 1947].

[15] $A(\ldots)$ in (2) is two-way attenuation of the radiation in the mantle

$$A(\varepsilon_M, \tan\delta, H, \theta') = \exp(-4\pi \cdot \tan\delta \cdot \sqrt{\varepsilon_M} \cdot H/\cos\theta' \cdot \lambda), \quad (4)$$

where λ is the wavelength, and $\tan\delta$ is the loss tangent of the mantle material.

[16] The scattering coefficient at the mantle-substrate interface $U(\varepsilon_S/\varepsilon_M,\xi_S,\theta')$ (2) depends on the relative dielectric permittivity of $\varepsilon_S/\varepsilon_M$, the incidence angle θ' of radiation inside the mantle, and the substrate roughness ξ_S. The radar echo from the unmantled surface (Figure 2b) is defined totally by $U(\varepsilon_S,\xi_S,\theta)$. Here we assumed that substrate scattering $U(\ldots)$ is described by the mean radar backscattering function for Venus derived by *Muhleman* [1964] with

coefficients specified by *Pettengill et al.* [1988] considering a mean permittivity of the Venus surface equal to 4.5. Following several authors [e.g., *Ulaby et al.*, 1986; *Tyler et al.*, 1992], we considered also that the substrate scattering function is proportional to the square of the Fresnel coefficient at normal incidence $U(\varepsilon_S,\xi_S,\theta) \sim R(\varepsilon_S,0)^2$. With such an assumption, we can recalculate the radar cross section of a typical unmantled surface into the scattering coefficient at the substrate-mantle interface, taking into account the difference in the normal Fresnel reflection coefficient (due to the change of relative dielectric permittivity from ε_S to $\varepsilon_S/\varepsilon_M$), and new incidence angle of radiation in the mantle θ'.

[17] In general, the darker appearance of parabolas in radar images, in comparison with their surroundings, according to (1), can potentially be caused by attenuation (4) of radiation inside the mantle itself, and/or by a smoother upper interface of the mantled surface: $\xi_M < \xi_S$ for thick mantles, and/or by lower mantle dielectric permittivity $\varepsilon_M < \varepsilon_S$.

[18] Several lines of evidence suggest that the mantle-atmosphere interface in the DDFs is smooth at the wavelength scale. The strongest argument comes from the Arecibo dual polarization radar observations. *Carter et al.* [2004] have reported on the detection of a nonzero linear polarization of the radar echo for a circularly polarized probing signal for a number of DDFs. This indicates that the mantle-atmosphere interface is smooth in these locations.

[19] Thick, smooth (at wavelength scale) mantles can cause complete absorption of throughgoing incident radiation $A(\ldots) \approx 0$ (4), so $F(\ldots) \approx 0$ (2). In such cases only the mantle-atmosphere interface can form a radar echo (1). A surface covered by a thick mantle with a smooth upper interface $\xi_M \approx 0$ will give no radar response at all. On Venus we found an area with a possibly very thick and smooth (at wavelength scale) mantle located between craters Greenaway, Ban Zhao, and Callirhoe (21°N, 142.7°E) that could be formed from overlapping deposits from these craters [*Schaller and Melosh*, 1998]. Values of the specific radar cross section in the area are very close to those expected from thermal noise (12.7 dB below the planetary average). This observation can be considered as another piece of evidence that DDF mantles are smooth at the wavelength scale.

[20] According to the Fraunhofer criterion, a surface can be considered smooth if a standard deviation of the surface height σ_H is lower than $\lambda/32\cos\theta$ [*Ulaby et al.*, 1986]. Thus for the Magellan wavelength of observation (λ = 12.6 cm), DDF mantles could be considered smooth if they are characterized by σ_H lower than 4.4–5.6 mm, respectively, for incidence angles of 25°–45° (the majority of SAR observations).

[21] Mantles with a smooth upper surface will effectively decrease the radar cross section only if they are homogeneous at the scale relevant to the wavelength of the probing signal. In particular, this homogeneity puts an upper boundary on the size of particles that form the mantle: particles should be smaller than the size corresponding to the resonance scattering region [e.g., *Ulaby et al.*, 1986]. This gives the following constraint on particle size r:

$$2\pi r|\varepsilon|^{0.5}\lambda^{-1} < 0.5, \quad (5)$$

where λ is the wavelength of observation, and ε is the relative dielectric permittivity of the particle material. Calculations show that sizes should be smaller than 3.2–4 mm (corresponding to dielectric permittivities from 10 to 6, as is typical for terrestrial dry bedrock [*Campbell and Ulrichs*, 1969]). This observational constraint means that the material forming the DDF mantles should be made of coarse sand or finer particulate material.

[22] Analysis of size distribution of clasts in deposits from 26 km crater Ries and 100 km crater Popigai on Earth presented in [*Basilevsky et al.*, 2004] shows that if fragmentation and comminution of the parabola-forming ejecta was similar to that of terrestrial allogenic breccias and suevites, then the deposits may be dominated by particles smaller 1 mm.

[23] The approach based on the attenuation of radio waves in the mantle has been used for estimation of the dune size [e.g., *Arvidson et al.*, 1992], as well as for some mantle depth estimations [e.g., *Campbell et al.*, 1992; *Bondarenko and Head*, 2004].

[24] The model presented here does not consider multiple bouncing of the radiation between interfaces inside the mantle; estimations show that this contribution is small enough to be neglected. The model also does not take into account interference effects; for a mantle of appreciable thickness (compared to the wavelength) these effects could average out owing to the inevitable variations in the mantle thickness.

2.2. Aging Process

[25] For the study of possible aging processes it is very important to understand the starting point: the initial state of young DDFs. A detailed study of the specific properties of dark parabolas (young DDFs), including root-mean-square (rms) slopes, scattering asymmetry, and mantle dielectric permittivity, is presented in section 3.

[26] The efficiency of the actual aging process that could alter distal crater deposits is as yet unknown. We can hypothesize two end-members of mantle aging processes leading to elimination of their initial radar-dark appearance: (1) mantle material remains at the sites of deposition but becomes radar brighter (owing to changes of the mantle physical properties or structure) and (2) mantle material is removed from the parabola area by winds.

[27] In the first end-member, the alteration could occur owing to the interaction with the high-temperature, high-pressure chemically reactive Venus atmosphere. We can suppose a variety of possible mechanisms of alteration. For example, chemical modification and weathering has been widely discussed by a number of authors [e.g., *Wood*, 1997; *Brackett et al.*, 1995; *Fegley et al.*, 1997]. Owing to the presumably high porosity of the mantles, atmosphere-caused alteration could not only occur at the very surface of the mantle, but also rather uniformly within its interior volume, and could lead to a change in the bulk properties of the mantle, preserving (or not preserving) the smooth mantle-atmosphere interface.

[28] These processes could lead to changes in the electromagnetic properties of the mantle material, for example, through changes in the density or mineralogy. This could affect the dielectric permittivity, which in turn influences the scattering properties and electromagnetic losses. In general,

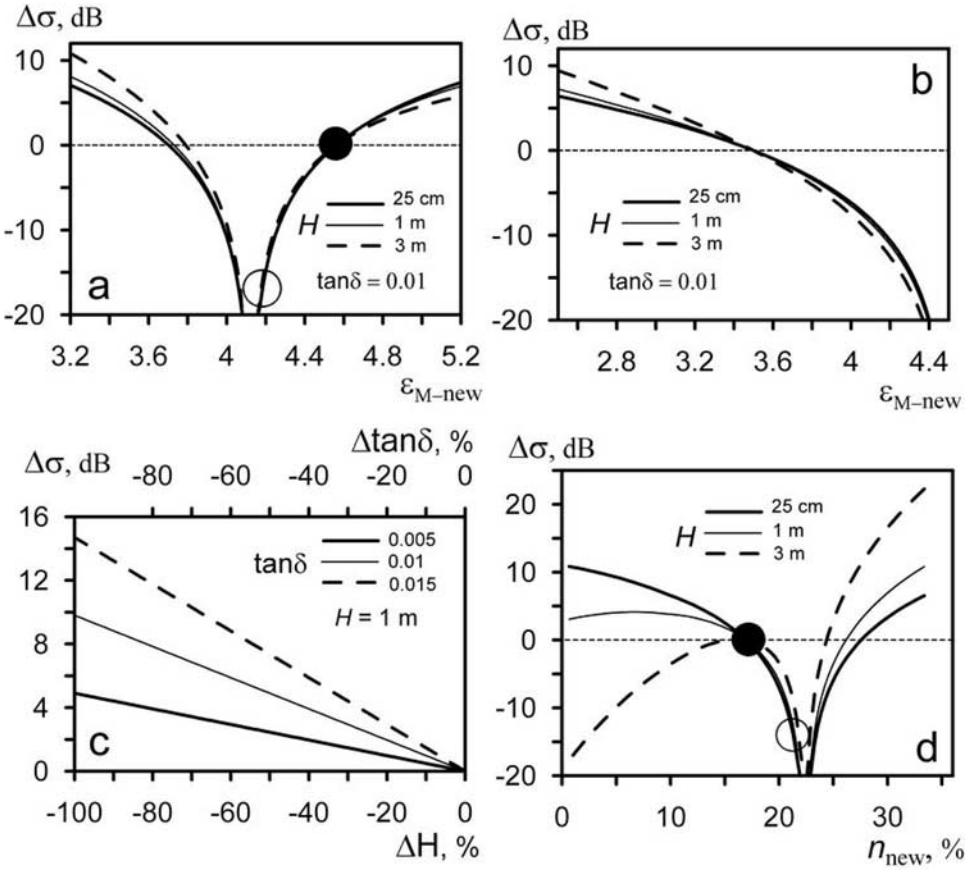

Figure 3. Expected change of radar brightness $\Delta\sigma$ of mantled surface with smooth (at wavelength scale) upper interface due to the change of initial mantle properties versus (a) new mantle dielectric permittivity $\varepsilon_{M\text{-}new}$ (initial mantle properties: $\varepsilon_M = 4.56$, $\tan\delta = 0.01$, mantle thickness $H = 25$ cm, 1 m, and 3 m; substrate permittivity $\varepsilon_S = 4.12$); (b) new mantle dielectric permittivity $\varepsilon_{M\text{-}new}$ (initial mantle properties: $\varepsilon_M = 3.5$, $\tan\delta = 0.01$, mantle thickness $H = 25$ cm, 1 m, and 3 m; substrate permittivity $\varepsilon_S = 4.5$); (c) relative change of mantle thickness ΔH (bottom abscissa axis), and mantle loss factor $\tan\delta$ (top abscissa axis); (d) new mantle density $\rho_{M\text{-}new}$ (initial mantle density $\rho_M = 2.48$ g cm^3). Solid circle corresponds to the initial mantle state, and open circle corresponds to a state with ε_M decreased to 4.24.

the decrease of mantle electromagnetic losses and the smooth (at the wavelength scale) upper mantle interface can result in an apparent sequential disappearance of the radar-dark signature of thinner mantles and the shrinking of the recognizable area of DDFs.

[29] We estimated how the expected radar brightness can be changed owing to a change of mantle thickness and bulk mantle properties, including dielectric permittivity, loss factor, and porosity using model (1) and considering a flat upper mantle surface as a simulation for a smooth (at the wavelength scale) mantle-atmosphere interface. The change of mantle bulk physical properties influences the mantle attenuation factor, transmission of radiation through the upper mantle boundary, and the scattering coefficient from the lower mantle-substrate interface (2). To make these estimates, we assumed an incidence angle $\theta = 45°$, typical for low latitudes in the first cycle of Magellan radar images.

[30] Results of calculations are shown in Figure 3. The expected change of radar brightness $\Delta\sigma$ was obtained as the ratio of the radar cross section of the mantled surface calculated using new mantle properties σ_{new} with respect to the radar cross section of the mantled surface in its initial state σ_{initial}:

$$\Delta\sigma = \frac{\sigma_{new}}{\sigma_{initial}}. \tag{6}$$

We test here two options for different initial relationships between the substrate and mantle permittivity. For the first case the initial values of mantle and substrate permittivity were chosen to be $\varepsilon_M = 4.56$ and $\varepsilon_S = 4.12$. These values correspond to the mean dielectric permittivity of dark parabola material and the average permittivity of typical terrains in the vicinity of craters of 30 km–70 km range, as shown in section 5. The permittivity of typical terrains $\varepsilon_S = 4.12$ coincides also with the mean dielectric permittivity for Venus plains of 4.0–4.5 as reported by *Ford and Pettengill* [1992].

[31] The change of observed radar cross section versus the new mantle dielectric permittivity is presented in Figure 3a. Calculations were made for three values of mantle thickness: 25 cm (thick solid line), 1 m (thin solid line), and 3 m (dash line). The same value of 0.01 for the

loss factor tanδ was maintained, a value that is typical for dry powdered materials [e.g., *Campbell and Ulrichs*, 1969]. The initial state of the radar-dark mantled surface is marked in Figure 3 with a solid circle. Figure 3a shows that decrease of the mantle initial permittivity down to 4.12 (as for ε_S) leads to a sequentially darker appearance of the mantled surface. This occurs owing to a decrease of the scattering efficiency at the substrate/mantle interface. In contrast, an increase of initial mantle permittivity in this case leads to a brightening of the mantled surface.

[32] We also study the case in which the mantle permittivity is lower than the permittivity of underlying surface ($\varepsilon_M < \varepsilon_S$). Initial values of the mantle and substrate permittivity were chosen to be, respectively, $\varepsilon_M = 3.5$ (as derived for the parabola of crater Ban Zao from Magellan emissivity data [*Bondarenko and Head*, 2004]) and $\varepsilon_S = 4.5$. The change of the expected radar cross section based on the new mantle dielectric permittivity values for mantles with thicknesses of 25 cm, 1 m, and 3 m, is shown in Figure 3b. In this case such a change of mantled surface radar appearance follows simple rules: the lower the mantle permittivity, the higher radar cross section, and vice versa.

[33] The decrease of the mantle material loss factor or the decrease of mantle thickness lessens the absorption in the mantle (4) and thus brightens the mantled surface. Examples are shown in Figure 3c. Calculations were made using mantle and substrate permittivity of $\varepsilon_M = 4.56$ and $\varepsilon_S = 4.12$. Initial mantle thickness was taken to be 1 m. In Figure 3c the change of radar cross section is plotted versus the relative change of mantle thickness (bottom abscissa axis) for different initial loss factors: 0.005 (thick solid line), 0.01 (thin solid line), and 0.015 (dash line). Figure 3c shows that the removal of mantles with a higher loss factor is the most efficient process for mantle brightening.

[34] The same curves in Figure 3c show the change of radar cross section versus the change of the mantle loss factor (top abscissa axis) relative to its initial value: 0.005 (thick solid line), 0.01 (thin solid line), and 0.015 (dash line). In order to cause noticeable brightening of a dark mantled surface, the initial mantle loss factor has to decrease rather significantly. For example, to brighten the mantle by 8 dB (such a difference is often observed between DP and pure surface [*Bondarenko and Head*, 2004]) the mantle loss factor has to decrease by 50%.

[35] Both the dielectric permittivity and the loss factor of the particulate material are known to depend on material density [*Campbell and Ulrichs*, 1969; *Ulaby et al.*, 1986; *Carrier et al.*, 1991]. In terms of material porosity, *n,* this means that the higher the porosity, the lower the dielectric permittivity and the lower the loss factor. To illustrate this, we used empirically derived relationships between dielectric properties and density from *Carrier et al.* [1991]

$$\varepsilon = 1.843^{\rho_M}, \quad \tan\delta = 10^{0.398\rho_M - 2.871}, \quad \rho_M = \rho_0(1-n), \quad (7)$$

where n is mantle material porosity, ρ_M and ρ_0 are porous mantle material and the same solid material density, respectively. The density of solid material was considered to be 3.0 g cm^{-3} as for terrestrial rocks, and the initial mantle porosity was chosen to be 0.17. This value of mantle porosity corresponds to initial mantle permittivity of 4.56 and to a mantle loss factor of 0.013 (7). Substrate permittivity was $\varepsilon_S = 4.12$. The dependence of the change of radar cross section on the new mantle porosity is presented in Figure 3d for mantles of different thickness: 25 cm (thick solid line), 1 m (thin solid line), and 3 m (dash line). The behavior of curves shown in Figure 3d is similar to those shown in Figure 3a. Radar brightening can begin only when the mantle porosity increases by ~10% or above ~60% of its initial value. Radar brightening can occur also if mantle porosity decreases and the mantle is rather thin.

[36] Chemical weathering could lead to the lithification of loose mantles as suggested by *Basilevsky et al.* [2004]. This hypothesis is supported by the low-bearing capacity of the uppermost layer of the Venus surface measured during landings of the Venera 9, 10, 13, and 14 spacecraft, which point to porous material comparable with terrestrial tuff. Partly lithified parabola deposits also can be responsible for layered rocks seen in Venera panoramas [*Basilevsky et al.*, 2004]. A lithified mantle could undergo a variety of modification processes, for example, erosion by winds that could increase the surface roughness. Tectonic processes would also cause cracking and structural roughening of lithified mantles. Loose deposits can also be roughened by wind action owing to formation of dunes or ripples. Roughened loose deposits, in turn, could be lithified subsequently.

[37] Surface small-scale roughness (<12 cm as for Magellan observations) including edges, cracks, rocks, and any surface inhomogeneities, causes diffuse scattering which controls radar backscattering on Venus at oblique angles [e.g., *Pettengill et al.*, 1988]. When the mantle-atmosphere interface roughens, scattering at this interface $S(\varepsilon_M, \xi_M, \theta)$ (1) increases, and the substrate becomes relatively less visible (Figure 4a). The net effect of the roughening of the upper mantle surface is to increase the radar brightness at oblique angles during SAR observations. This effect can be weakened by a possible decrease of mantle permittivity, but surface roughening seems to be more important. For example, calculations based on a small perturbation model [*Ulaby et al.*, 1986] presented by *Campbell et al.* [1992] show the same specific radar cross section for surfaces having $\varepsilon = 4.0$ along with rms slope $\xi = 8.2°$, and $\varepsilon = 3.0$ along with $\xi = 9.6°$ (for all incidence angles used during Magellan SAR observations). This means that mantle permittivity has to decrease by 25% to compensate for the 17% increase of surface slopes.

[38] The portion of the radar echo from the mantle-substrate interface can also decrease if aging processes lead to formation of sequentially coarser particles inside the mantle. Such an option is supported by the possibility for particle-to-particle adhesion under Venus surface conditions as discussed by [*Marshall et al.*, 1991]. When size of growing particles exceeds the lower limit of the resonance scattering region (5), particles can turn out to be effective scatterers. Thus the mantle becomes heterogeneous and volume scattering has to be taken into account. A diagram illustrating this possibility is shown in Figure 4b.

[39] If an older (aged) roughened mantle has the same roughness as a typical background surface, but a still higher porosity (to match the observations of Venera landers [e.g., *Kemurdzhian et al.*, 1983]), the mantle would still be darker than the typical surface owing to its lower mantle dielectric permittivity. For example, an old mantle with dielectric permittivity of 3.8 will be 1 dB darker than the pristine

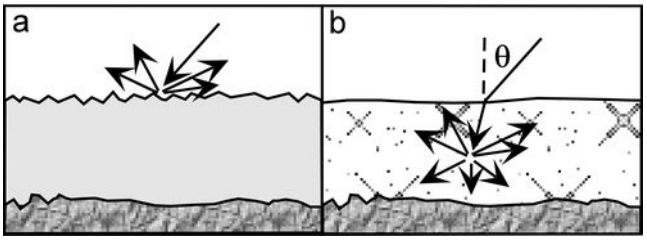

Figure 4. Sketches illustrating the source of the major portion of radar echo from old mantles: (a) rough mantle-atmosphere interface; (b) volume scattering.

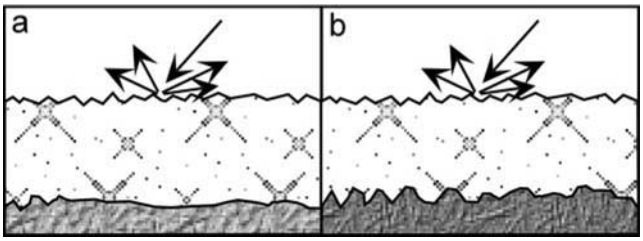

Figure 5. Sketches illustrating the radar backscatter from areas (a) A and (b) B covered by thick old brightened mantle. Areas A and B differ from each other by roughness and dielectric properties.

surface (with dielectric permittivity of 4.5) if both of them have the same upper surface structure. This estimate is based on the expected proportionality between the radar cross section and the surface normal Fresnel reflection coefficient.

[40] Thus, all the options discussed for the aging of extended crater-related mantles remaining at the site of deposition lead to a variety of possible appearances of old thick mantles, including bright, partly dark, or apparent invisibility.

[41] The rms height variation of terrestrial radar analogs for Venus plains is on the order of 2–10 cm at the horizontal scale of 1 m [*Shepard et al.*, 2001]. To cover such surfaces completely, parabola mantles have to be thicker than 10 cm. Mantles of this thickness are predicted for rather large portions of dark parabola areas near large craters (for example, for the crater Bassi shown by *Schaller and Melosh* [1998]). The area of observed crater dark parabolas varies from 24,000 km^2 for the crater Audrey (D = 15 km), up to 2,630,000 km^2 for the crater Greenaway (D = 89 km) [*Campbell et al.*, 1992]. Therefore, large areas, composed of subareas with different radar properties, are expected to be totally covered by even distant deposits of the crater.

[42] In general, if we consider that old mantles are still located at their sites of initial deposition and that aging processes result in brightening of dark parabola mantles, we can expect the presence of altered or brightened parabolic features on the Venus surface near old craters. If such a mantle is rather thick (at least thicker than 10 cm) and the mantle became bright, for example, owing to a rough atmosphere-mantle interface (Figure 4a) and/or increased mantle volume scattering (Figure 4b), then the underlying surface is expected to be unrecognizable. This can lead to apparent disappearance of boundaries between adjacent areas with different roughness and dielectric properties (Figures 5a and 5b). The examination of old brightened mantles at their sites of initial deposition using such an approach is discussed in section 4.

[43] In the second end-member of mantle aging processes, mantle material is removed from the parabola area by winds. Winds start working on dark parabola material from the time of initial deposition. Wind action can lead to a decreasing of mantle thickness (area A, Figure 6) and/or concentration of mantles in local surface depressions (area B, Figure 6). Winds can also redistribute particulate material and transport it over rather long distances. This often leads to formation of aeolian features which have an asymmetric shape (area C, Figure 6), such as dunes, ripples, accumulation of material in wind shadows (area D, Figure 6), etc. Unresolved asymmetric features on Venus have been recognized in the radar data on the basis of the difference between the strengths of the radar echo when probing from opposite sides at similar incidence angles [e.g., *Weitz et al.*, 1994; *Tyler et al.*, 1992; *Bondarenko et al.*, 2006]. For example, if a steep dune slope is normal to incident radiation $\theta_R = 0$ for an observation from the right (area C, Figure 6), this leads to a much higher radar echo in comparison with the observation from the left. The gentle dune slope faces in the upwind direction [e.g., *Greeley et al.*, 1997]. Our study of the E-W and N-S scattering asymmetry of DDFs is discussed in section 5.

3. Young Extended Crater Deposits

3.1. Parabolic Shapes

[44] Impact craters with radar-dark extended parabolic deposits occupy the uppermost stratigraphic position relative to their surroundings [*Campbell et al.*, 1992] and are among the youngest features and geological units on the surface of Venus [e.g., *Basilevsky and Head*, 1995]. The total number of craters with dark parabolas is about 10% of the entire crater population. Their ages are estimated not to exceed 0.1T, where T is the mean Venus surface age [e.g., *Arvidson et al.*, 1992]. The parabolic shapes of the more distant deposits are formed owing to the interaction of the expanding ejecta plume with the Venus atmosphere. The atmosphere can transfer particles ejected during impact to high altitudes and transfer them long distances from the source [*Vervack and Melosh*, 1992; *Campbell et al.*, 1992]. DDF shape remains parabolic only for young craters and is presumably destroyed with time.

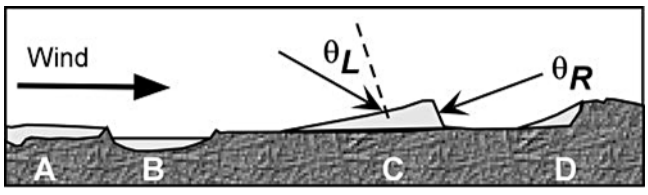

Figure 6. Sketches illustrating results of DDF mantle erosion by winds. Area A is thin deposits, area B is remains of mantles in surface depression, area C is dune, and area D is accumulation of material in wind shadows. Incidence angles for observations from the right and from the left are θ_R and θ_L, respectively. Dashed line shows local normal to the gentle dune slope. Thick arrow indicates downwind direction.

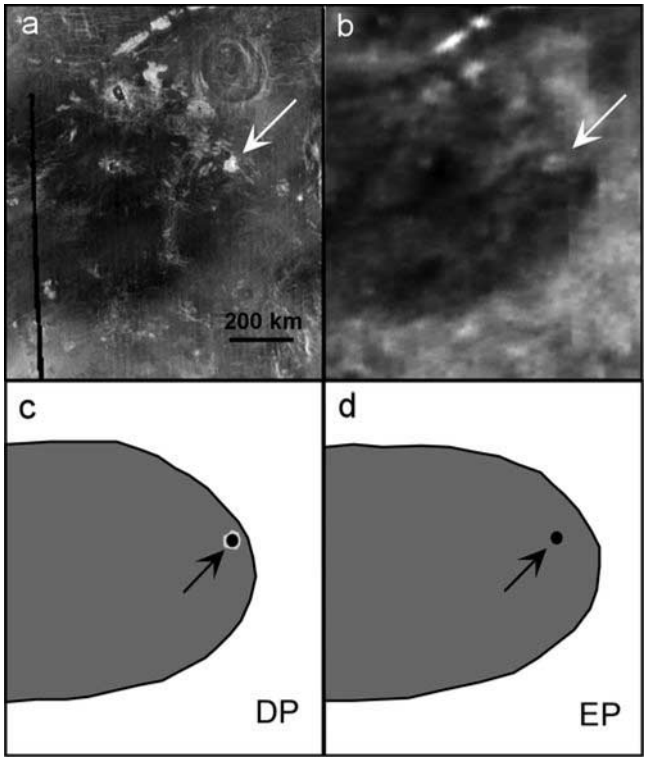

Figure 7. Emissivity feature of the parabolic type associated with the crater Li Quingzhao (23.7°N, 94.6°E; D = 22.4 km). (a) Synthetic aperture radar (SAR image); radar-dark parabola is seen, (b) emissivity map, (c) sketch of the dark parabola (DP) (Figure 7a), (d) sketch of the emissivity parabola (EP) (Figure 7b). See Figure 1 for legend.

[45] In emissivity maps obtained as part of the Magellan radiometry experiment [*Pettengill et al.*, 1992] there are 27 low-emissivity parabolic features associated with craters [*Bondarenko and Head*, 2004]. Fourteen of these craters (Glaspell, Eudocia, Akeley, Frank, Abington, du Chatelet, Nadine, Noreen, Merit Ptah, Philomena, Rose, Li Quingzhao, Kodu, and Lyon) also have radar-dark parabolas. Low-emissivity features are wider than the corresponding radar-dark parabolas, indicating that the crater-related deposits are significantly wider than is apparent from the DDFs alone [*Bondarenko and Head*, 2004]. A similar conclusion was reached by *Carter et al.* [2004] from interpretation of Earth-based polarimetric radar observations. The other 13 emissivity parabolas are not seen in SAR images at all, or exhibit only partial signatures with irregularly shaped DDFs, perhaps owing to the presence of very thin mantles [*Bondarenko and Head*, 2004]. The parabolic shape of low-emissivity features points to a rather young age for these extended crater deposits poorly observed in radar images. For example, the 22.4 km diameter crater Li Quingzhao (23.7°N, 94.6°E), shown in Figure 7, is characterized by parabolic shapes of both the associated radar-dark deposits and the low-emissivity feature.

3.2. RMS Slopes

[46] We systematically studied rms slopes of the radar-dark surfaces surrounding craters associated with parabolas that are listed in the works by *Campbell et al.* [1992], *Basilevsky and Head* [2006] and the crater database of R. Herrick (http://www.lpi.usra.edu/research/vc/vchome.html) using the map of rms slopes (decameter-scale roughness, GXDR data set) derived from the Magellan radar altimeter data [*Ford and Pettengill*, 1992]. We considered the area around each crater extending to 20 crater diameters in each direction from the crater center. Any surface in the SAR image with a radar cross section lower than the planetary average for the same incidence angle [*Pettengill et al.*, 1988] was considered as a "dark" surface. Such a "wide" approach allows us to include areas covered by thin mantles in this study. Local DDFs surrounding smaller craters within the areas of the larger deposit were excluded from the analysis.

[47] The mean rms slopes ξ calculated over radar-dark surfaces around 41 craters is shown in Table 2. ξ is related to Hagfors' decameter-scale roughness parameter C as $\xi = 1/\sqrt{C}$. For 29 parabolas the mean rms slopes are lower than the typical rms slopes reported for regional plains (2.5°–4.5°) [*Garvin et al.*, 1985]. Since we do not know the precise values of radar cross sections that separate pure and mantled surfaces at every crater location, estimates of rms slopes shown in Table 2 can be biased by areas that are slightly darker in comparison with "mean" surface due to intrinsic reasons, but are not mantled. The lowest rms slopes (0.87°, Table 2) characterize the dark parabola of the crater Boleyn shown in Figure 8. Lower rms slopes (darker in Figure 8c) correspond to the darkest parabola parts observed in the radar mosaics (Figure 8a). The coarsest parabolas belong to craters Stowe, Glaspell and Eudocia.

[48] The crater Eudocia exhibits an extended parabola with high rms slopes covering the vicinity of the crater Guan Daosheng. Its size is ~1900 km in the E-W direction, a value that is 73 times larger than the crater diameter. The roughness parabola is accompanied by a high Fresnel reflectivity parabola. The dielectric permittivity of the parabola material (see section 3.4) here reaches values of up to 20. The crater Eudocia is also characterized by a wide and extended low-emissivity parabola, which is about twice as wide as the roughness parabola.

[49] For comparison the average rms slopes of typical Venus surfaces observed in the vicinity of each of the craters under study (closer than 20 crater diameters) are also shown in Table 2. Such typical surfaces are chosen to have radar cross sections equal to or not higher than 2 dB from the planetary average as described in [*Pettengill et al.*, 1988]. Usually, rms slopes of a typical surface are higher than rms slopes of dark surfaces near DP craters. However, five craters, namely Caldwell, Bassi, Carson, Sabin, and Stowe, show the opposite relationship.

[50] No dependence between crater sizes and associated radar-dark parabola rms slopes was found. For example, dark parabolas of the 80 km crater Stowe and the 27.7 km crater Glaspell exhibit rather high rms slope values (~2.9°). In turn, dark parabolas of the 68.6 km crater Stuart and the 38.3 km crater Ban Zhao have characteristics similar to each other and rather low rms slope values (~1.4°).

3.3. Asymmetry

[51] *Bondarenko et al.* [2006] analyzed the backscattering asymmetry in the north–south (N-S) direction using Doppler centroid data from the SCVDR data set derived from the

Table 2. Properties of Radar-Dark and Typical Surfaces Near Parabola Craters[a]

				ξ (deg)		f_D (kHz)			ε[b]		ε[c]			
											Dark			
												Lowest 10%		
Name	Latitude (°N)	Longitude (°E)	D (km)	Dark	Typical	Dark	Typical	$\Delta\sigma$, dB (dark)	Dark	Typical	Whole	σ	ξ	Typical
Boleyn	24.4	220.1	70.4	0.87	1.57	−0.405	−0.241	−3.7	4.53	4.05	2.80	2.87	2.95	2.75
Stuart	−30.8	20.2	68.6	1.40	2.36	0.204	0.203	−3.3	4.24	4.07	3.99	4.14	4.23	4.12
Ban Zhao	17.2	146.9	38.3	1.42	2.66	−0.165	−0.340	−5.4	4.27	3.69	3.07	3.07	3.20	2.88
Akeley	8.0	244.5	22.7	1.60	1.87	0.073	−0.122	−3.5	4.93	4.10	4.28	4.57	4.25	3.85
Holiday	−46.7	12.9	26.3	1.62	2.35	−0.713	−0.634	−3.2	4.01	3.85	4.10	4.23	4.24	4.12
Von Schuurman	−5.0	191	28.9	1.62	2.08	0.057	0.093	−2.2	4.71	4.44	3.30	3.59	3.49	3.11
Audrey	23.8	348.1	15.3	1.65	2.20	−3.500	−3.056	−3.1	4.77	4.40	3.50	3.51	3.52	3.31
Barauka	10.6	346.3	12.8	1.67	2.06	−2.642	−0.394	−1.5	3.99	3.89	3.39	3.58	3.24	3.38
Aurelia	20.3	331.8	31.1	1.69	2.99	−2.086	−1.584	−3.0	3.99	3.74	3.30	3.38	3.30	3.05
Phyllis	12.2	132.4	10.6	1.69	2.02	−0.619	−0.928	−3.1	4.10	3.83	3.14	3.12	3.12	3.00
Ruth	43.3	19.9	17.9	1.71	2.38	0.007	−0.011	−2.7	4.54	4.23	3.45	3.61	3.50	3.36
Himiko	19.0	124.3	36.7	1.79	2.28	−0.747	−0.947	−4.1	4.27	3.91	3.00	3.32	3.28	2.99
Comnena	1.2	343.7	19.0	1.80	2.23	−0.566	−0.374	−3.1	3.77	3.55	3.35	3.39	3.53	3.40
Li Quingzhao	23.7	94.6	22.4	1.86	2.32	−0.030	−0.209	−3.6	5.35	4.64	3.85	4.04	3.87	3.62
Noreen	33.6	22.7	18.2	1.86	2.14	−0.521	−0.493	−3.6	4.78	4.24	3.68	4.01	3.68	3.46
Rose	−35.2	248.2	14.7	1.90	2.29	0.083	0.190	−2.1	5.91	4.90	5.22	5.69	4.82	4.66
Adivar	8.9	76.2	30.3	1.98	2.63	−0.273	−0.307	−4.8	4.95	3.99	3.71	4.02	3.84	3.52
Sitwell	16.6	190.4	31.9	2.00	2.72	−0.298	−0.328	−1.8	4.44	4.35	2.86	2.82	2.67	2.99
Caldwell	23.7	112.4	51.0	2.01	1.85	−0.631	−0.639	−4.5	4.82	4.53	3.43	3.57	3.58	3.32
Frank	−13.1	12.9	22.6	2.02	2.15	−0.314	0.065	−2.7	5.08	4.48	4.10	4.54	3.93	3.86
Boulanger	−26.6	99.3	71.5	2.05	2.80	0.208	0.354	−3.5	4.38	4.12	3.80	3.79	4.00	3.65
Philomena	−40.7	151.9	14.9	2.05	2.52	0.270	0.129	−2.0	4.00	3.78	4.07	4.34	4.28	4.00
Annia Faustina	22.1	4.7	22.4	2.06	2.39	−1.084	−1.092	−3.2	4.07	3.75	3.34	3.10	3.50	3.29
Bassi	−19.0	64.7	31.4	2.32	1.86	0.178	0.384	−2.3	4.53	4.17	3.76	3.62	3.82	3.80
Du Chatelet	21.5	165.0	19.0	2.34	2.48	−0.080	−0.294	−2.0	4.84	4.20	3.69	4.04	3.57	3.38
Abington	−47.8	277.7	22.6	2.43	2.94	−0.520	−0.627	−3.0	4.66	4.11	4.55	4.59	4.43	4.25
Nadine	7.8	359.1	18.8	2.43	2.47	−0.899	−0.503	−2.6	4.09	3.76	3.65	3.76	3.45	3.48
Kodu	0.9	338.7	10.8	2.47	2.65	0.618	0.671	−2.3	4.17	3.77	3.84	4.08	3.60	3.64
Nadisha	−39.1	97.2	11.3	2.47	2.86	0.203	0.500	−1.7	3.88	3.90	3.81	4.18	3.63	3.72
Hayasi	53.8	243.9	43.1	2.53	2.90	−0.161	−0.119	−2.5	4.43	4.158	4.15	3.45	3.57	3.43
Merit Ptah	11.4	115.6	17.0	2.53	2.65	−0.273	−0.325	−3.4	4.93	4.44	3.54	3.60	3.51	3.30
Yablochkina	48.3	195.3	64.3	2.55	2.58	−0.052	−0.228	−3.8	5.20	4.31	3.59	3.72	3.68	3.29
Carson	−24.2	344.1	38.8	2.57	2.56	−0.033	−0.233	−2.9	4.85	4.01	4.45	4.86	4.21	3.96
Adaiah	−47.3	253.4	17.5	2.61	2.84	−0.575	−0.714	−2.4	4.81	4.52	4.74	4.83	4.55	4.54
Sabin	−38.5	274.7	33.1	2.61	1.75	0.473	0.28	−3.7	4.40	4.27	3.92	3.88	3.98	4.08
Magnani	58.6	337.2	26.6	2.62	2.72	−7.728	−7.481	−2.3	4.22	3.83	3.79	4.09	3.49	3.63
Martinez	−11.7	174.7	23.1	2.62	2.88	0.718	0.558	−2.6	4.48	4.20	3.29	3.55	3.57	2.98
Akiko	30.6	187.3	17.1	2.68	2.79	−0.168	−0.271	−2.5	3.83	3.70	2.63	2.56	2.58	2.58
Stowe	−43.2	233.2	80.0	2.91	2.37	−1.529	−1.502	−2.7	5.25	4.92	4.70	4.97	4.70	4.67
Glaspell	−58.5	269.6	27.7	2.93	3.11	−1.232	−1.758	−2.1	4.96	4.51	4.50	4.43	4.50	4.34
Eudocia	−59.1	202.0	25.9	4.02	4.48	−1.501	−0.799	−2.0	6.98	6.69	5.25	5.48	5.27	4.87

[a] D, crater diameters; ξ, average rms slope; f_D, average value of Doppler centroid; $\Delta\sigma$, average specific radar cross section relative to the planetary average described by *Pettengill et al.* [1988]; ε, average real part of dielectric permittivity; dark, surface with a specific radar cross section lower than the planetary average described by *Pettengill et al.* [1988]; typical, surface with variations of specific radar cross section 0 – +2 dB from the planetary average described by *Pettengill et al.* [1988]; whole, the whole dark surface; lowest 10%, the 10% portion of the dark surface with lowest values of specific radar cross section (σ) and rms slopes (ξ).

[b] Fresnel reflectivity.

[c] Emissivity data with Fresnel equation.

Magellan radar altimeter experiment [*Tyler et al.*, 1992]. They reported that the majority of recognized crater dark parabolas and dark halos show no such asymmetry, while in other terrains the asymmetry is ubiquitous. This finding was interpreted as one piece of evidence for smooth (at the decameter scale) mantle-atmosphere interfaces [*Bondarenko et al.*, 2006]. The resolution of the Doppler centroid map is rather poor, ~50 km, so only large craters can be seen there. The extended deposits from these craters are expected to be among the thickest on Venus. Figure 9 shows one of the best examples of the absence of dark parabola scattering asymmetry around the crater Bassi in the Doppler centroid map (inset). This parabola is smooth, has no N-S asymmetry at the decameter scale, and covers a background surface with a pronounced N-S slope asymmetry. A similar N-S symmetric scattering is characteristic of the radar-dark halo of the crater Elena (marked with an arrow in Figure 9). Values of the mean Doppler centroid calculated over radar-dark and typical surfaces surrounding the parabola craters are shown in Table 2. The majority of dark parabolas are characterized by nearly symmetric scattering: their mean Doppler centroid is within the ±0.93 kHz interval, which corresponds to the precision of individual Doppler centroid measurements [*Tyler et al.*, 1992].

[52] However, eight dark parabolas, including the three roughest parabolas (craters Stowe, Glaspell, and Eudocia), exhibit a distinctive scattering asymmetry in the N-S direction at the decameter scale. Such scattering asymmetry can

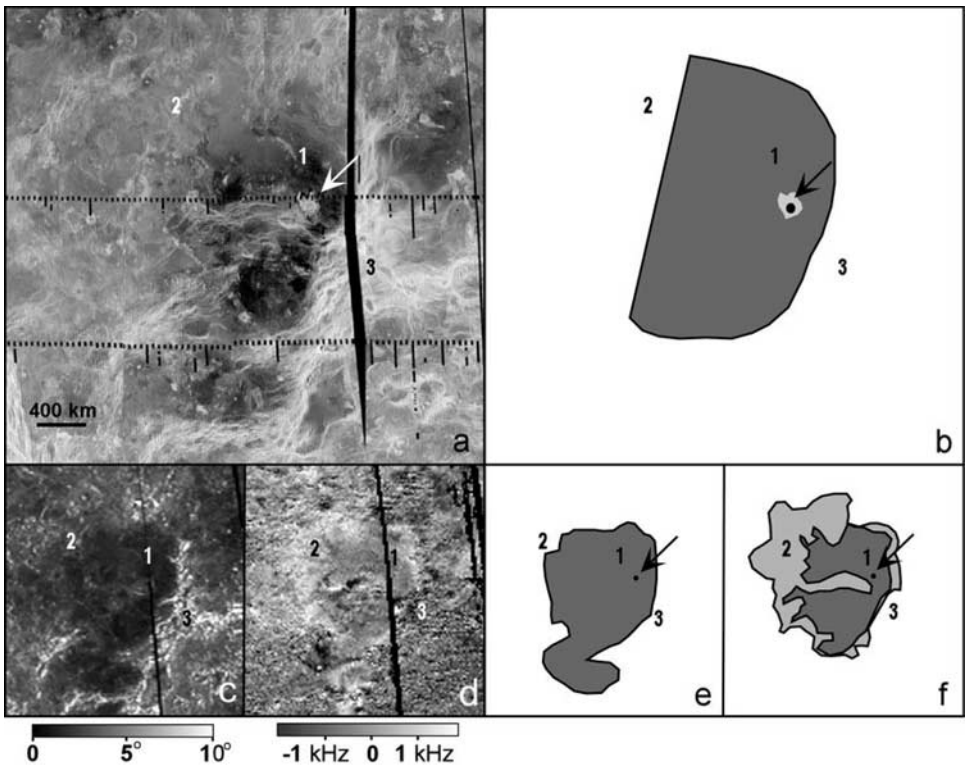

Figure 8. The crater Boleyn (24.4°N, 220.1°E, D = 69 km): (a) SAR image, (b) sketch of the dark parabola of the crater (Figure 8a; see Figure 1 caption), (c) rms slopes map, (d) Doppler centroid map, (e) sketch of the low RMS slopes (dark gray) area (Figure 8c), (f) sketch of the Doppler centroid map (Figure 8d) (dark gray, symmetric scattering; light gray, high anisotropy). The 1 is inner parabola part; 2 is outer parabola part; 3 is fracture belt. Arrows show crater location.

be caused by small-scale roughness asymmetry of the surface [*Bondarenko et al.*, 2006]. Additionally, craters Stuart, Caldwell, Annia, Faustina, and Stowe are characterized by a similar N-S scattering asymmetry for both radar-dark and typical surfaces.

[53] Some areas in the southwest part of the parabola near the crater Stowe are known to exhibit asymmetric scattering in an east–west direction [*Weitz et al.*, 1994]. This asymmetry was interpreted to be caused by microdune fields [*Weitz et al.*, 1994] that can be responsible for a rougher mantle-atmosphere interface.

[54] The observed variations of parabola large-scale and small-scale roughness can be attributed to specific aspects of mantling in each case, including variations in underlying surface properties, as well as the nature and amount of ejected material. The roughness differences can also be caused by aging processes associated with dark parabolas.

3.4. Permittivity

[55] Table 2 also contains average values for the dielectric permittivity of the dark parabola material. The permittivity was derived using Fresnel reflectivity data obtained in the Magellan radar altimeter experiment. For comparison, Table 2 also lists the average dielectric permittivity of typical surfaces outside the parabolas. Table 2 shows that the permittivity of parabola material is systematically higher than permittivity of the typical "bright" surface nearby. Such higher values vary from 0.09 (crater Sitwell) up to 0.96 (crater Adivar) in terms of permittivity. These values become 2% and 24%, respectively relative to the permittivity of the "typical" surface.

[56] In addition to dielectric permittivity derived from the radar altimeter data, Table 2 lists dielectric permittivity derived from Magellan microwave emissivity measurements. In general, the emissivity measurements are characterized by a larger (compared to the altimeter) footprint of ~20 km. Microwave emissivity is affected by large-scale and small-scale roughness of the mantle-atmosphere interface. For rough surfaces, emissivity-derived estimates of permittivity would be underestimated. To lessen this spurious effect, in addition to the average permittivity of dark surfaces, we calculated the permittivity for its smoothest parts. We outlined the smoothest parts in two ways: we took 10% of the parabola area with the lowest rms slope, which gives the lowest large-scale roughness, and 10% with the lowest radar cross section, which gives the lowest small-scale roughness.

[57] In general, dielectric permittivity derived from the emissivity data follows the same trend as the permittivity derived from the altimeter data: it is higher for dark surfaces than for typical surfaces, with five exceptions, namely, the craters Stuart, Bassi, Sabin, Holiday, and Comnena. If we consider the permittivity of the smoothest at small- and large-scale surfaces, only the crater Sabin falls out of the trend. The difference in emissivity-derived permittivity between dark and typical surfaces varies from 0.01 to 0.56. This difference is lower than one derived from the altimeter data.

[58] For craters with diameters >30 km (Table 2) average parabola dielectric permittivity (from the altimeter data) is

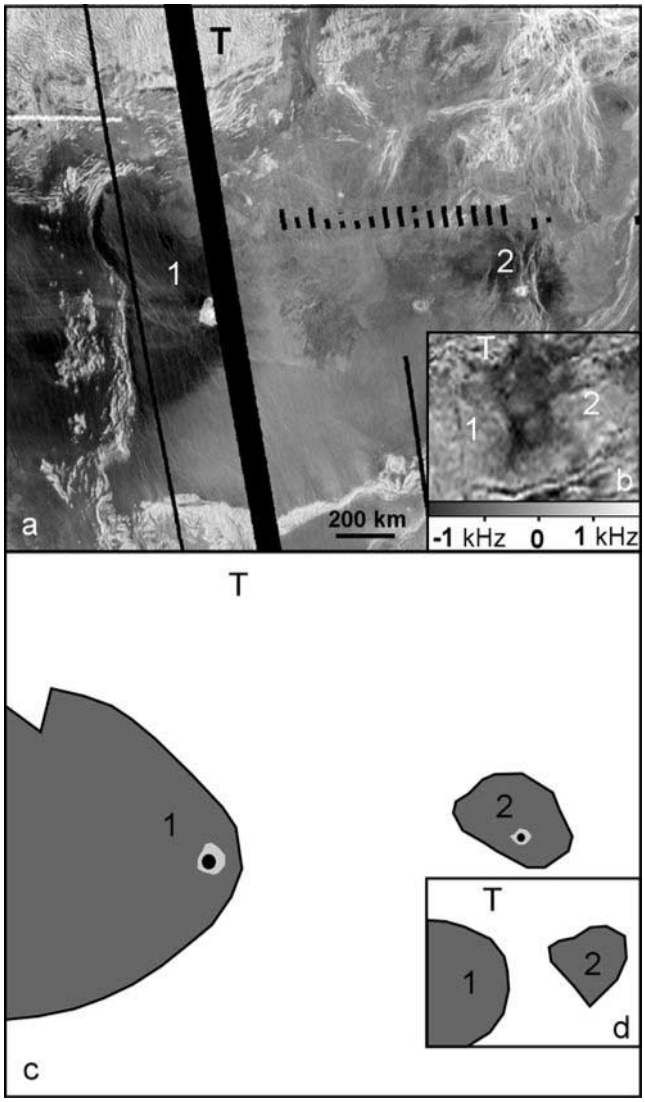

Figure 9. Magellan SAR mosaic of the crater Bassi (19°S, 64.7°E, D = 35 km, marked as 1) and its vicinity. (a) SAR image, (b) the Doppler centroid map of the same area, (c) sketch of the radar-dark deposits (dark gray), (d) sketch of the DDF associated zero Doppler centroid (dark gray). The 2 is dark halo crater Elena; T is Ovda Tessera.

4.56 ± 0.34 (range: 3.99–5.25) while the average permittivity of a typical surface nearby is 4.15 ± 0.30 (range: 3.69–4.92).

[59] If the mantle density of DDFs is ~2.3 g cm^{-3} (a value typical for densely packed media formed by spheres of the same radius with solid rock density of 3.0 g cm^{-3} [*Carrier et al.*, 1991]), a DDF material dielectric permittivity of 4.56 leads to a permittivity of 8.3 for rocks. The Rayleigh mixing formula [*Campbell and Ulrichs*, 1969] was used for these calculations. Dielectric permittivity of 7–9 is observed for dry solid terrestrial basalt [*Campbell and Ulrichs*, 1969].

3.5. Summary

[60] Generally, the typical state of young dark parabola mantles seems to be that they are characterized by a smooth (at wavelength scale and decameter scale) mantle-atmosphere interface. The permittivity of parabola material is systematically higher than permittivity of the typical bright surface nearby. The higher dielectric permittivity of dark surfaces can be related to the higher initial permittivity of deep rocks excavated during impacts. It can also reflect a lower level of weathering experienced by the parabola material owing to their rather recent formation.

4. Old Craters and Their Vicinities

[61] Craters that do not exhibit any radar-dark diffuse features in their immediate surroundings are usually considered to be old. This has been confirmed by analysis of volcanically embayed and tectonically deformed craters [*Izenberg et al.*, 1994]. The diversity of target terrains and the limited crater population on Venus do not allow a robust statistical approach to the study of DDF mantled surfaces hypothetically modified by age. Instead, we systematically studied the surroundings of 31 large (>30 km) craters without any associated radar-dark features nearby and 23 large craters having faint dark halos. We used the radar images in places where a parabola would be expected to search for diffused disappearance of boundaries of underlying volcanic units and any features that could be interpreted as altered or brightened parabolas considering that old mantles are still located at their sites of initial deposition and that aging processes result in brightening of dark parabola mantles, as discussed in section 2.2. We found only a few examples of each kind.

4.1. Diffused Disappearance of Boundaries

[62] The crater Deken (47.1°N, 288.5°E, D = 48 km) (Figure 10) has several minor dark diffuse areas close to the crater rim. Poorly resolved boundaries between lava flows are located ~400 km northwest from the crater (marked with white dashed lines in Figure 10b) and are ~150 km in length. An arrow in Figure 10b points to the apparent disappearance of the boundary. These boundaries are also shown with white dotted lines in the emissivity map (Figure 10d). Dark areas marked with W and Z in Figure 10b exhibit high emissivity. The southeast part of area *W* seems to be modified by material brought in from its southeast.

[63] Figure 10c shows at higher resolution the area outlined with the black dashed line in Figure 10b. We compared different available data for the two areas ("X" and "Y") outlined with white dashed lines in Figure 10c, on both sides of the diffuse boundary. Area Y is part of a brighter feature that looks like a wide brightened wind streak. Table 3 presents the mean values over X and Y of radar cross section $\Delta\sigma$ relative to the Muhleman law, rms slope ξ, Fresnel reflectivity R_0, and emissivity E; all are very close to each other. This suggests similar surface structure and material in both areas, possibly residual mantle material redistributed by wind.

4.2. Remnants of Altered and/or Brightened Mantles

[64] Volcanic shields marked with "A" and "B" in the vicinity of crater Nijinskaya (25.8°N, l22.5°E, D = 35.4 km; radar looking angle is 43.5°) (Figure 11) are brighter than the surroundings by 1.4 dB to 2.2 dB. For the shields

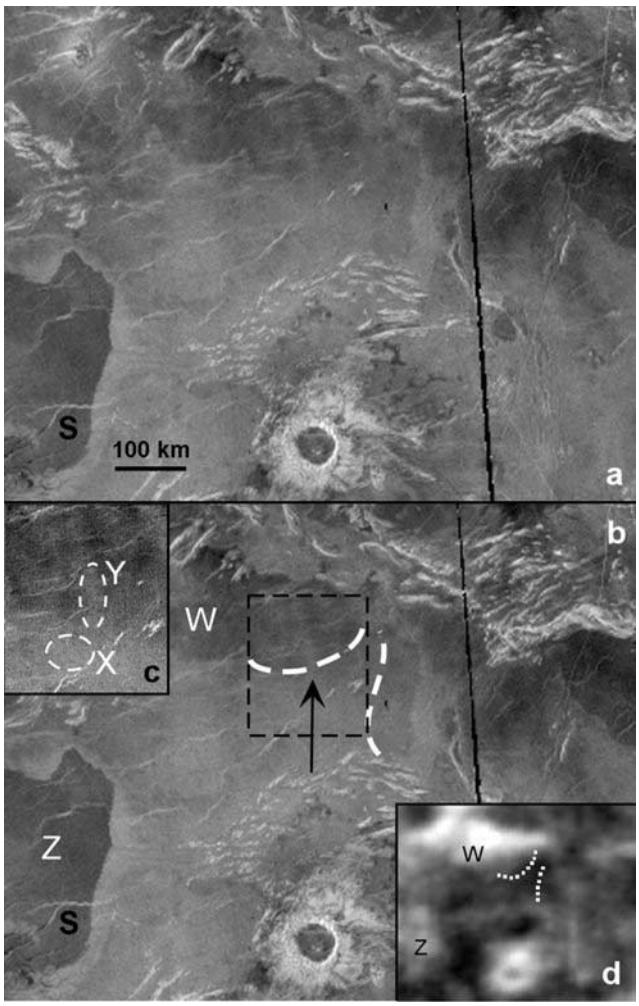

Figure 10. The crater Deken (47.1°N, 288.5°E, D = 48 km): (a) SAR image, (b) SAR image with subtle boundaries marked by dashed line, (c) high-resolution SAR image of rectangle marked in Figure 10b, (d) emissivity map. X and Y are areas apparently related to the same surficial deposit, Z and W are radar-dark lava flows seen as bright areas in the emissivity map. Arrow points to the place of apparent disappearance of the boundary. S marks the area with dark deposits accumulated along ridges.

marked with "C," which are located to the west of the crater (in the place where the extinct parabola should have been), the difference is lower, 1.0 dB. We suggest that these shields and/or close terrain have a partial surface coverage by brightened distal deposits from the crater Nijinskaya. Sizes of shields in the "C" area are ~25 km in diameter.

[65] The surface near the crater Chiyojo (47.8°S, 95.7°E, D = 38.8 km) is shown in Figure 12. Radar contrasts between lava flows at sites marked with C and D (1.4 dB and 1.2 dB, respectively) to the west of the crater are lower, in comparison with radar contrasts at A and B (2.4 dB and 2.2 dB, respectively). The distance between C and D sites is ~100 km. The surface shown in Figure 12 exhibits a similar appearance and radar cross section during the first and second Magellan cycles (24° and 25.2° incidence angles, respectively).

Table 3. Observed Properties for Sites Marked With X and Y in Figure 10c[a]

Site	$\Delta\sigma$ (dB)	ξ (deg)	R_0	E
X	1.53 ± 0.21	2.3 ± 0.2	0.12 ± 0.005	0.854 ± 0.0006
Y	1.31 ± 0.19	2.6 ± 0.3	0.12 ± 0.002	0.859 ± 0.0028

[a] $\Delta\sigma$, average specific radar cross section relative to the planetary average described by *Pettengill et al.* [1988]; ξ, average rms slope; R_0, average Fresnel reflectivity; E, average emissivity.

[66] A dark area located southwest of the crater Agnesi (39.5°S, 37.7°E, D = 41.4 km) has different radar contrasts along the boundary with the same flow (marked with a "W" in Figure 13). Its eastern boundary between B and C (closer to the crater) appears to be poorly resolved. Radar contrasts here are 0.8–1.5 dB, while at position A the radar contrast increases to 3.2 dB. The surfaces on both sides of the B-C boundary exhibit similar emissivity, RMS slope, Fresnel reflectivity. Length of B-C part of the boundary is ~70 km.

[67] The surface south of the crater Rhys (8.6°N, 298.8°E, D = 44.0 km) (Figure 14) looks rather homogeneous. However, the large diffuse area marked with an A is ~2.4 dB darker compared with area B, further from the crater. The extent of this diffuse area can be traced in Figure 14b (dark gray color). Figure 14b was obtained by processing of the radar image shown in Figure 14a. The diffuse boundary between the A and B areas and the boundary location (not farther than ~10 crater radii) are consistent with the possible presence of aged distal crater

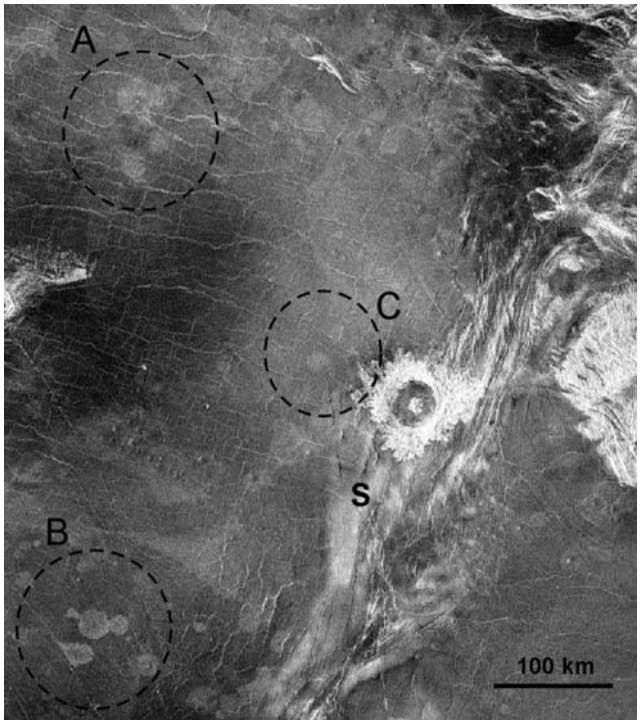

Figure 11. The crater Nijinskaya (25.8°N, 122.5°E, D = 35.4 km). SAR brightness contrasts between volcanic shields and surroundings are 1.4 dB, 2.2 dB, and 1.0 dB in sites A, B and C, respectively. S marks the area with dark deposits accumulated along ridges.

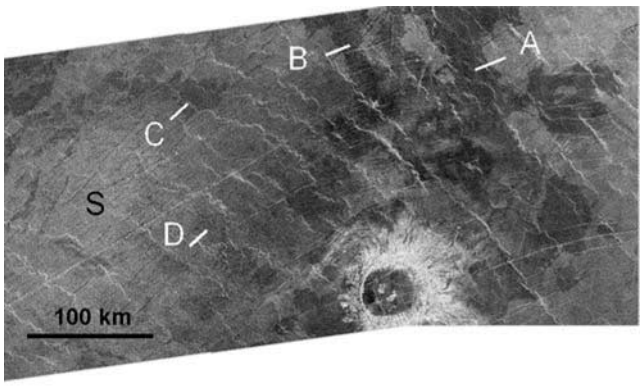

Figure 12. The crater Chiyojo (47.8°S, 95.7°E, D = 38.8 km). SAR brightness contrasts across unit boundaries at sites marked with A, B, C, and D are 2.4 dB, 2.2 dB, 1.4 dB, and 1.2 dB, respectively. S marks the area with dark deposits accumulated along ridges.

deposits in the area A. The length of diffuse boundary marked with dark dash line in Figure 14b is ~100 km. Area A and B are characterized by rms slopes of 2.2° and 3.1°, and dielectric permittivity values of 3.45 and 4, respectively.

4.3. Surface Images

[68] It is possible that lithified extended deposits from the crater Sanger, modified by tectonic processes, are seen in the Venera 9 panorama (the panorama is shown by *Florensky et al.* [1977]). However, the landing site location is poorly known. Within the known confidence circle [*Weitz and Basilevsky*, 1993], the Venera 9 landing site is closer than 100–500 km eastward from the craters Sanger (D = 83.8 km) and Letitia (D = 17.2 km), 200–600 km south of the crater Lenore (D = 14.8 km), 600–1000 km west of the crater Patty (D = 46.5 km), and 300–700 km west of the crater Wazata (D = 13.9 km). Craters as large as Sanger, namely Stuart (D = 69 km), Boulanger (D = 72 km) and Greenaway (D = 92 km), have parabolas with eastward extensions of 198–468 km. Hence, we expect that thick (>10 cm) deposits can be found in close proximity to these craters.

[69] The other landers are located much further away from their closest craters. For example, the closest crater to the Venera 14 landing site is located at a distance of about 160–500 km to the west (the crater Ingrid, D = 13.9 km). For craters of similar diameter, the observed eastward parabola extent does not exceed ~95 km [*Schaller and Melosh*, 1998].

4.4. Other Observations

[70] A general observation made in the vicinity of old craters is the presence of a number of radar-dark deposits westward from craters seen in association with small topographic features and along ridges. The abundance of such features in any surface area depends on the particular geological structure. For example, in the vicinity of old craters discussed above, deposits in wind shadows are marked with S as follows: in the left-bottom image part, westward from crater Deken in Figures 10a and 10b; southward from "C" area in Figure 11; many deposits along ridges through the entire area but a more dense

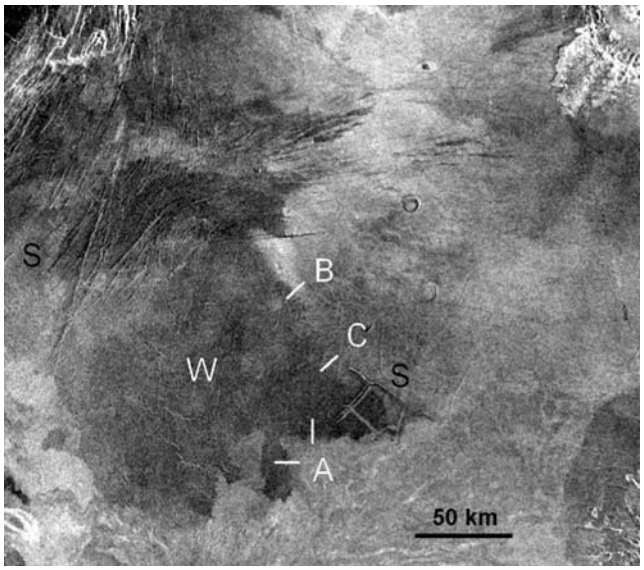

Figure 13. The crater Agnesi (39.5°S, 37.7°E, D = 41.4 km). SAR brightness contrasts across unit boundaries at sites marked with A, B, and C are 3.2 dB, 0.8 dB, and 1.5 dB, respectively. S marks the area with dark deposits accumulated along ridges.

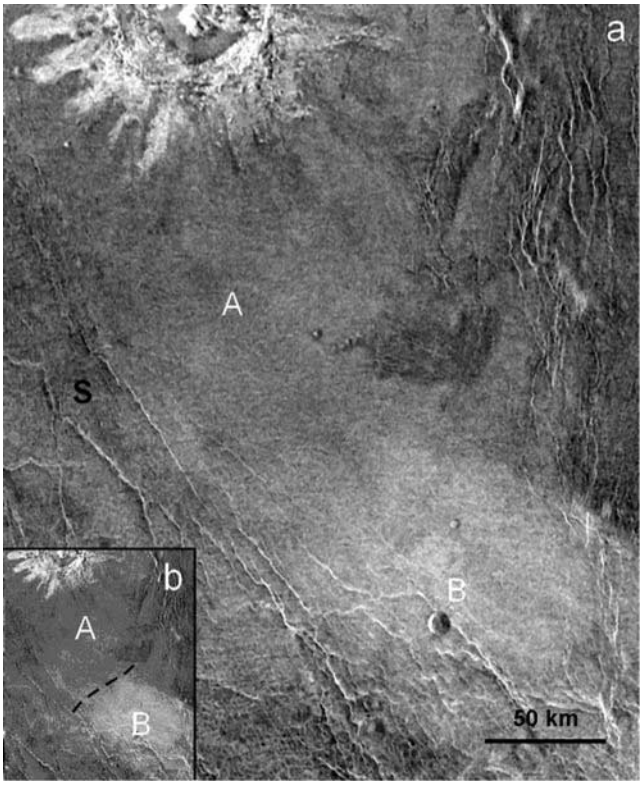

Figure 14. The crater Rhys (8.6°N, 298.8°E, D = 44.0 km): (a) SAR image, (b) extent of area A as seen after processing of image (Figure 14a). Dashed line shows the location of diffuse boundary between units A and B. SAR brightness difference between sites A and B is ~2.4 dB. S marks the area with dark deposits accumulated along ridges.

appearance westward from the crater Chiyojo in Figure 12; west–southward and westward from the crater Agnesi in Figure 13; close to the crater Rhys (~70 km) in Figure 14.

[71] Such features were widely reported earlier [*Arvidson et al.*, 1992; *Greeley et al.*, 1995]. It was also shown that many surface wind streaks observed (~32% from all known) tend to occur in association with parabolic ejecta deposits [*Greeley et al.*, 1997].

[72] The volume of ejected loose material that formed distant crater deposits from all impacts was estimated to be enough to explain all of the particulate material seen on the surface of Venus [*Garvin*, 1990; *Vervack and Melosh*, 1992]. Another possible source of loose material, erosion of rocks due to particles moving by winds, seems to be a rather slow process because the dense Venus atmosphere leads to a reduction of the local eolian erosion rate [*Williams and Greeley*, 1994].

4.5. Summary

[73] The limited number of candidates for thick weathered distant crater deposits (5 from 54) means that mantling by ancient dark parabola material is not widespread on Venus. Thick mantles seem not to retain their DDF properties over the whole area of initial mantle deposition. Terrains where parabolas formerly existed are now still characterized by different microwave properties. We conclude that thick aged mantles seem not to remain in the sites of deposition.

5. DDF Scattering Anisotropy as a Signature of Wind Erosion

[74] Scattering anisotropy in the east–west and the north–south directions has been observed in many areas on the surface of Venus [*Weitz et al.*, 1994; *Kreslavsky and Vdovichenko*, 1999; *Bondarenko et al.*, 2006]. Scattering anisotropy is interpreted to be related to an asymmetry in the surface roughness, which is caused by small-scale asymmetric features like dunes, ripples, etc., formed owing to reworking of loose material by winds or deposition of loose material in wind shadows.

[75] Winds on the surface of Venus can redistribute particulate material and transport it over rather long distances. There are numerous wind streaks on the surface of Venus and many examples of dark material in wind shadows [*Greeley et al.*, 1997; *Kreslavsky and Vdovichenko*, 1999]. Two large dune fields (Aglaonice and Fortuna-Meshkenet) were found in SAR mosaics and are associated with loose material from the crater Aglaonice and from the craters La Fayette jointly with Jadviga, respectively [*Weitz et al.*, 1994]. These fields show a distinct asymmetry in the east–west direction. Three areas of very strong E-W asymmetry (the observed difference is up to 8 dB), and interpreted as microdune fields [*Weitz et al.*, 1994], are localized in the western parts of parabolas near craters Stowe, Eudocia and Guan Daosheng. Widespread weaker scattering anisotropy over the plains of Venus has been reported by *Kreslavsky and Vdovichenko* [1999] and *Bondarenko et al.* [2006]. These have been interpreted to represent the widespread occurrence of eolian features, perhaps, microdunes.

[76] We reviewed right- and left-looking radar observations, focusing on craters with DDFs and on the DDFs themselves. We analyzed in detail about 50 craters of different sizes using Magellan first cycle (east-looking geometry, angles of observation: 20.5°–27.5°) and second cycle (west-looking geometry, angles of incidence: 24.2°–25.3°) radar images in the 40°S–60°S latitude zone. Seven craters situated in the 7°N–22°N latitude zone were studied using second cycle (west-looking geometry, incidence angle 24.9°) and third cycle (east-looking geometry, incidence angle 25.2°–25.6°) Magellan images.

[77] The majority of DDFs studied exhibit a similar (dark) appearance in observations from both sides. In results similar to *Weitz et al.* [1994], we found a scattering asymmetry of ~1–4 dB associated with radar-dark diffuse areas west of several small craters, including Adaiah (52.2°S, 111.2°E, 18 km) and Abigail (27.3°S, 253.4°E, 19 km). A relatively brighter diffuse area in the SSW direction at ~100 km from the flow crater Xiao Hong (43.6°S, 101.7°E, 37.6 km), is darker in the second cycle, by 1.0–1.8 dB, compared to the first cycle of observation. This surficial deposit is rather large and is superposed on several boundaries between volcanic plain units.

[78] The N-S roughness asymmetry of DDFs was studied using the Doppler centroid map [*Bondarenko et al.*, 2006] (for details see section 3.3). In many areas on Venus, the strongest surface echo is systematically deflected from the nadir; the Doppler centroid quantifies such deflection [*Tyler et al.*, 1992]. In the plains, values of Doppler centroid are a measure of scattering anisotropy in the north–south (N-S) direction, related to surface relief asymmetry at scales from centimeters to hundreds of meters. The effective spatial resolution of the Doppler centroid map is rather poor: ~50 km in the 20°S–40°N latitude zone, and only allows the study of large DDFs.

[79] We studied 46 large craters (>30 km) with associated DDFs located in the 20°S–40°N latitude zone. We also detected several smaller DDF craters clearly recognized in the Doppler centroid map. We found that the radar-dark parabolas and well-expressed halos are usually associated with areas of zero Doppler centroid (N-S symmetric roughness). The mean values of the Doppler centroid calculated over dark surfaces near parabola craters are shown in Table 2.

[80] The low decameter-scale roughness of parabolas and halos seen in the Magellan rms slope map (GXDR data set), and the dominantly symmetric scattering in both N-S and E-W directions, support the interpretation of the DDFs as surficial deposits with smooth (at large scale and small scale) and possibly flat upper surfaces [*Campbell et al.*, 1992; *Bondarenko and Head*, 2004].

[81] The most remarkable features associated with DDFs found in the Doppler centroid map are bands of a distinctively high degree of N-S roughness asymmetry, along the outer parts of parabolas near the craters Boleyn (24.4°S 220.1°E, 69.8 km) and du Chatele (21.5°S 165.0°E, 19 km). The SAR image of the crater Boleyn and a part of the Doppler centroid map for the same area are shown in Figures 8a and 8d. The bright band (marked with "2") coincides with plain areas without any signature in the radar image. The observed bands of increased asymmetry at the periphery of the crater-related deposit indicate wind reworking of the deposit material in the areas where deposits are thin. This asymmetry coincides with microdune shapes

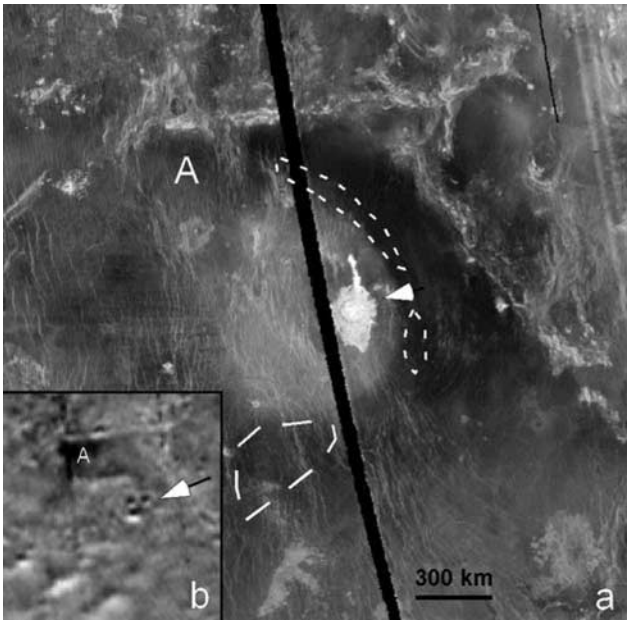

Figure 15. The crater Stowe (43.2°S, 233.2°E, D = 75.3 km): (a) SAR image; (b) Doppler centroid map. Doppler centroid in area A varies from −0.5 Hz down to −2.1 Hz.

formed by equatorward surface winds prevalent in the northern hemisphere of Venus [*Bondarenko et al.*, 2006]. The map of the rms slopes for the crater Boleyn area is shown in Figure 8c. The center part of the parabola shows both low rms slope and symmetric N-S scattering. The radar-darker surfaces surrounding the crater Boleyn have the lowest rms slopes in comparison to those for other parabola craters (Table 2). The band with higher N-S asymmetry in Figure 8d has no distinctive signature in the rms slopes map (Figure 8c).

[82] One more interesting finding in the Doppler centroid map is an area with negative values, coinciding with the northern part of the parabola of the crater Stowe, marked with A in Figure 15. Figure 15a shows a SAR image and part of the Doppler centroid map (Figure 15b) for the crater Stowe and its vicinity. The value of the Doppler centroid in area A varies from −0.5 Hz down to −2.1 Hz. Negative values of Doppler centroid mean longer south-facing slopes, as was shown by *Tyler et al.* [1992] and can be caused by microdunes built by equatorward surface winds prevalent in the southern hemisphere of Venus [*Bondarenko et al.*, 2006].

[83] The crater Stowe (43.2°S, 233.0°E, 80 km) was reported by *Weitz et al.* [1994] to exhibit scattering asymmetry caused by unresolved microdunes in the area outlined by the long dashed line in Figure 15a. Detailed study of this parabola shows that the outer eastward parabola segment does not exhibit EW asymmetry, while some areas marked with short dashed lines are characterized by scattering asymmetry in the inner and northwest parts of the parabola. The dark parabola surrounding the crater Stowe is one of the two roughest mantles, according to Table 2. The crater Stowe is characterized by a scattering asymmetry of parts of the parabola (hypothetically rather thin) in both E-W and N-S directions, that indicate a high level of wind erosion of parabola material.

[84] The study of scattering asymmetry shows that the majority of DDFs associated with craters are characterized by symmetric scattering in the E-W and N-S directions. In several places we see evidence for reworking and possible removal of parabola material by winds. These asymmetric aeolian features are located in the outer parts of radar-dark features where mantles are presumably thinner.

6. DDF Aging Sequence

[85] The following sequence of craters: dark parabola (DP), dark halo (DH), patchy dark areas ("faint halo," FH), and no associated dark deposits ("no halo," NH), has been suggested to reflect an age progression of craters from young to old [*Izenberg et al.*, 1994; *Basilevsky and Head*, 2002a]. Examples of craters of these types are presented in Figure 1. The youngest DDFs (parabolas, DP), as shown above, are characterized by a mostly smooth (at small scale) mantle-atmosphere interface. We analyzed the smoothness (at both small and large scale) of dark material along the proposed aging sequence. We studied the properties of dark surfaces near craters in the 30 km to 70 km diameter range in the 50°S–55°N latitude band that permits the use of the highest-resolution Magellan altimeter data.

[86] The average rms slope (GXDR data set from the Magellan data collection in the NASA Planetary Data System) was calculated over dark areas and plotted in Figure 16 versus an average difference between observed

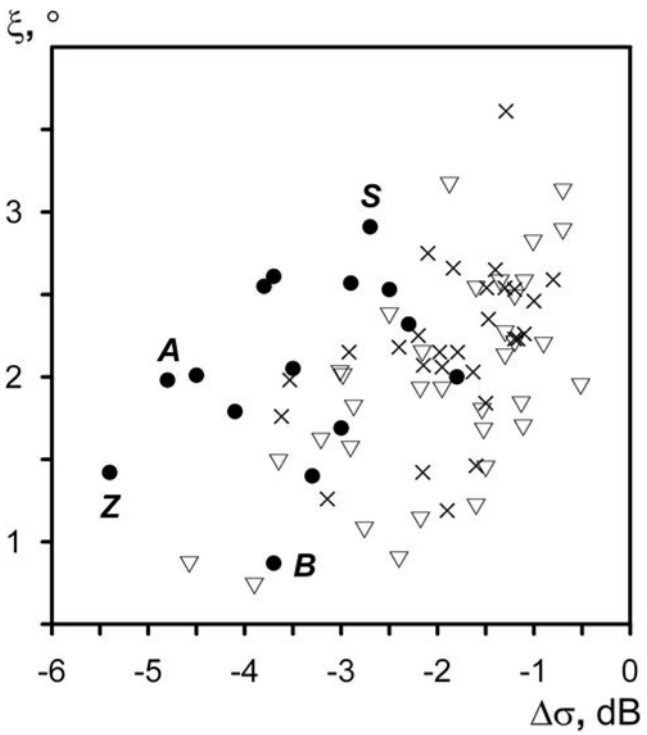

Figure 16. Mean rms slope ξ versus mean difference between observed radar cross section and the global average $\Delta\sigma$ for radar-dark areas near craters with dark parabola (solid circles), dark halo (crosses) and faint halo along with no halo (open triangles). A, B, S, and Z mark the dark parabolas of craters Adivar, Boleyn, Stowe, and Ban Zhao, respectively.

Table 4. RMS Slopes ξ of Typical and Dark Surfaces Near Craters[a]

		Typical Surface[b]		Dark Surface[b]		
Crater Type	Number of Craters	Mξ (deg)	ξ Limits (deg)	Mξ (deg)	ξ Limits (deg)	$\xi < 1.5°$, Surface Area[c]
DP	15	2.32 ± 0.46	1.57 – 2.99	2.07 ± 0.50	0.96 – 2.92	5.4% – 85.4%
DH	28	2.64 ± 0.48	1.75 – 3.62	2.18 ± 0.41	1.19 – 3.61	0.15% – 71.0%
FH	24	2.52 ± 0.43	1.66 – 3.23	2.10 ± 0.61	0.88 – 3.17	2.6% – 88.9%
NH	10	2.67 ± 0.56	1.9 – 3.86	1.92 ± 0.62	0.73 – 2.97	1.17% – 56.1%

[a]DP, dark parabola; DH, dark halo; FH, faint halo; NH, no dark material nearby; Mξ, average value of ξ and its rms deviation.
[b]For surface definition, see comments in Table 2.
[c]Proportion of the whole dark area.

radar cross section for the area and the global average described by *Pettengill et al.* [1988]. To define the dark surfaces, we used the same approach as described above in section 2. Dark surfaces near DP, DH and FH$^+$NH craters are shown in Figure 16 with dots, crosses, and open triangles, respectively. Generally, we see a wide scattering of the values of both parameters. The upper limit of observed average radar cross section $\langle\sigma\rangle$ is slightly higher sequentially for DH craters in comparison with DP craters and for FH craters in comparison with DH craters. The rms slope of dark material near DH and FH craters is similar and often lower in comparison with DP craters at the same radar brightness.

[87] As mentioned above rms slopes derived from Magellan altimeter data and SAR observations are related to different roughness scales. For the altimeter experiment, such a scale is from meters to tens of meters, while SAR radar cross section depends mostly on small-scale surface roughness (centimeters-decimeters). There is no strong general correlation between radar cross section and surface rms slopes in Figure 16. For all crater types rms slope tends to be higher for brighter objects in that the highest rms slope is observed for brighter objects.

[88] For DP craters (dots in Figure 16), higher values of rms slopes and/or small-scale roughness of parabola material could arise owing to, for example, microdune fields located in the outer thin parabola areas. For example, the parabola of the crater Stowe (marked with an S in Figure 16) is the roughest and also shows high roughness anisotropy that could be caused by asymmetric aeolian features on the surface. The parabola of the crater Adivar (marked with an A in Figure 16) is one of the darkest and is characterized by a rather high rms slope area, adjoining to the outer north parabola part (perhaps having thin deposits). The parabola of the crater Ban Zhao (marked with a Z in Figure 16) is the darkest in the set and is also not especially smooth at large scale. The parabola of the crater Boleyn (marked with a B in Figure 16) is the smoothest at large scale but not very dark and exhibits high roughness anisotropy in its outer parts.

[89] Furthermore, the tendency of higher rms slopes having brighter surfaces can occur owing to several different reasons. One possibility is that the average rms slope is biased owing to areas that are darker in comparison to a typical reference surface, but not mantled. In such cases, the higher average radar cross section means that we see a more pure surface. Another possibility is that the actual aging process (for example, erosion of lithified deposits) leads to simultaneous roughening at different scales. This could be the case for FH$^+$NH and DH craters (triangles and crosses in Figure 16).

[90] The rms slope ξ of dark and typical surfaces in the vicinity of the craters under study, averaged for craters of different types, is shown in Table 4 along with standard deviation and limits of variation. Typical surfaces are defined as having radar cross sections in the range from the planetary average up to 2 dB higher than the planetary average described by *Pettengill et al.* [1988]. In general, variations of rms slope for typical surfaces near craters of different types presented in Table 4 look rather similar to each other. Dark areas of different DDF types are also close to each other in terms of values of average rms slope and variation limits. However, the rms slope of dark surfaces is clearly lower than the rms slope of typical surfaces (Table 4).

[91] We also calculated the proportions of the lowest rms slope (<1.5°) surfaces in dark areas near craters. Such smooth (at large scale) surfaces are observed in the vicinity of each crater. In Table 4 the ranges of proportions of low rms slopes surfaces are presented for all DDF crater types. All types show a wide range of such proportions from parts of a percent up to tens of percent. This proportion may be related to the particular underlying terrain topography in the crater area. For old craters, low rms slopes and somewhat dark surfaces are widely observed. They may represent remnants of the mantles.

[92] Thus, all the observations described show that in the vicinity of any crater under study, including NH craters, there are areas darker in comparison with the mean surface of Venus. Dark surfaces near craters of any type usually are characterized by similar rms slope and always include regions with very low rms slopes. This may mean that the state and structure of dark material near craters are more or less similar for older mantles and for younger mantles.

[93] Values of average dielectric permittivity of dark and typical surfaces (as defined above) in the vicinity of craters of different types are presented in Table 5. Dielectric permittivity was derived using Fresnel reflectivity data from the Magellan altimeter experiment. Table 5 shows that typical surfaces in the surroundings of different type craters have similar dielectric permittivity values to each other. The average of the real part of the permittivity of dark mantle deposits exceeds that of the surrounding plains by 0.32 at a confidence level of 95%. Eighty-nine craters under study (out of 94) show a higher average permittivity for a dark surface in comparison with a typical one. Usually, the difference is not high and varies from 0.01 up to 1.4. The other five craters show the opposite relationship. These cases include one DH crater, Wen Shu (31.5 km, $\Delta\varepsilon = -0.72$), three FH craters, Germain (35.9 km, $\Delta\varepsilon = -0.93$), Romanskaya (30.4 km, $\Delta\varepsilon = -0.21$), Potter (46.9 km, $\Delta\varepsilon =$

Table 5. Dielectric Permittivity ε of Typical and Dark Surfaces Near Craters[a]

		Typical Surface[b]		Dark Surface[b]	
Crater Type	Number of Craters	Mε	ε Limits	Mε	ε Limits
DP	15	4.15 ± 0.30	3.69 – 4.92	4.56 ± 0.34	3.99 – 5.25
DH	28	4.09 ± 0.45	3.51 – 5.74	4.38 ± 0.49	3.61 – 5.90
FH	24	4.12 ± 0.42	3.30 – 5.27	4.38 ± 0.53	3.10 – 5.55
NH	10	4.12 ± 0.29	3.58 – 4.68	4.24 ± 0.36	3.58 – 5.21

[a]DP, dark parabola; DH, dark halo; FH, Faint Halo; NH, no dark material nearby; Mε, average value of ε with ε rms deviation.
[b]For surface definition see comments in Table 2.

-0.001), and one NH crater, Chiyojo (38.8 km, $\Delta\varepsilon = -0.06$). It is possible that the difference observed for crater Romanskaya occurs owing to the rather tectonized surrounding area, and for the crater Potter, owing to a nearby volcano. But the crater Chiyojo is old and exhibits the possible presence of old mantles, as discussed above.

[94] The dielectric permittivity of dark surfaces, on average, seems to be higher for DP craters in comparison with other types. The oldest NH craters are characterized by lower dielectric permittivity. Thus, all observations discussed show that aging of dark parabola material on Venus seems to be accompanied by decrease of its dielectric permittivity.

[95] Different aging processes affecting extended crater deposits (lithification, chemical weathering, aeolian erosion, etc.) start at the time of deposition. Since we did not find the widespread presence of thick (>10 cm) old brightened extended mantles, but observe much evidence for reworking of material on the surface of Venus by winds, including specific examples of the reworking of mantle material by winds, the rate of aeolian alteration seems to be higher in comparison with other aging processes.

[96] Temperatures on the surface of Venus lie above a critical thermal threshold that supports noticeable adhesion of surface material [*Marshall et al.*, 1991]. Particle-to-particle adhesion can cause an increase in the effective particle size inside the mantle; particle-to-underlying surface adhesion and partial welding could result in a growing accretionary layer. The latter might be responsible for the sequential attaching of mantle material to the underlying surface, and together with the removal of upper particles by winds, might explain the thin-layered structures of rocks observed at Venera -10, -13, and -14 landing sites rather far from possible source craters. Thin-layered structures of rocks observed in the Venera panoramas as mentioned above were interpreted by *Basilevsky et al.* [2004] to be caused by partial lithification of parabola deposits. Consolidation of particles inside the mantle (if it occurs) appears to allow them to be more efficiently removed by winds, but still prolong their movement by winds for a rather long time. This time may be comparable with the lifetime of parabolic features.

[97] The decrease of the dielectric permittivity of parabola material with age, together with similar large-scale and small-scale roughness properties of dark surfaces near all types of craters, means that parabola mantle cannot preserve its initial thickness. If they did, the old mantles for such a hypothetical case would be much darker than the initial one. To illustrate the expected change of radar cross section, a mantle with a dielectric permittivity of 4.24 (as for NH craters dark material) is marked with an open circle in Figures 3a and 3d.

[98] Thus the decrease of parabola material dielectric permittivity caused, for example, by chemical weathering, has to be accompanied by other physical processes that lead to noticeable brightening of the mantle. Such processes could include decrease of mantle loss factor or mantle thickness. These two parameters affect the absorption of radiation passing within the mantle. They appear as a product in (4) and their efficiency for brightening of the mantled surface based on relative change (Figure 3c) is the same.

[99] Commonly the loss factor of Earth dry material varying in the range from 0.01 to 0.03 has been used as a mantle loss factor to estimate the DDF thickness on Venus. Some lower values of mantle loss factor (0.001–0.005) were obtained on the basis of the scattering model for mantled surfaces [*Bondarenko and Head*, 2004] using the thickness of DDF near the crater Carson as predicted by [*Vervack and Melosh*, 1992]. The decrease in this small loss factor does not allow significant brightening of the mantled surface.

[100] On the other hand, several known meteorites, namely Bonita Springs, Forest City, and Indarch, have a significant iron content and exhibit much higher dielectric values and, in particular, loss factors of 0.065–0.22 [*Campbell and Ulrichs*, 1969]. If DDF mantles on Venus were rich in iron, the mantle material loss factor would be much higher and its decrease could be the most important factor for mantled surface brightening. This hypothesis leads additionally to thinner DDF mantles than those now considered.

[101] On the basis of our current knowledge, the decrease in mantle thickness caused by the removal of loose material by winds, which serves as a compensating factor for the radar darkening due to the decrease of mantle dielectric permittivity, seems to be the most efficient process responsible for degradation and removal of DDFs.

7. Conclusions

[102] 1. The majority of radar-dark parabolas on Venus are characterized by a smooth mantle-atmosphere interface having low rms slopes. Radar-dark halos also often have areas with low rms slopes of the upper mantle surface, possibly even flat. This means that the mantle can preserve its smoothness for a geologically long time, and that the wind action that leads to parabola degradation is slow on average at geological timescales.

[103] 2. Some parabolas and other DDFs have asymmetric small-scale relief formed as a result of wind action. This means that the mantle material can saltate under wind action, and is mobile.

[104] 3. There are a few examples of features that may be explained as a result of in situ modification of the mantle.

The rather small number of such places indicates that the regional and/or global redistribution of the loose material forming the mantles plays an important role in DDF modification and erosion.

[105] 4. Parabola aging processes are accompanied by a decrease of mantle material dielectric permittivity caused by chemical weathering and/or a decrease of mantle density which is equivalent to an increase of mantle porosity.

[106] **Acknowledgments.** We would like to thank P. Ford and R. Simpson for their comments that have considerably improved the quality of the paper and its organization. J.W.H. gratefully acknowledges support from the NASA Planetary Geology and Geophysics Program, grants NNG05G121G and NNX08AL47G.

References

Arvidson, R. E., R. Greeley, M. C. Malin, R. S. Saunders, N. Izenberg, J. J. Plaut, E. R. Stofan, and M. K. Shepard (1992), Surface modification of Venus as inferred from Magellan observations of plains, *J. Geophys. Res.*, *97*, 13,303–13,317.

Avduevsky, V. S., A. G. Godnev, Y. V. Zakharov, L. V. Petrosyan, V. V. Semenchenko, I. I. Syklyshkin, G. R. Uspensky, and Z. P. Cheremukhina (1983), An estimate of the physical and mechanical characteristics of the soil of Venus from measurements of the impact overload during the landing of the Venera 13 and Venera 14 automatic interplanetary stations, (in Russian), *Kosm. Issled.*, *21*, 171–175.

Basilevsky, A. T., and J. W. Head (1995), Regional and global stratigraphy of Venus: A preliminary assessment and implications for the geological history of Venus, *Planet. Space Sci.*, *43*, 1523–1553.

Basilevsky, A. T., and J. W. Head (2002a), Venus: Analysis of the degree of impact crater deposit degradation and assessment of its use for dating geological units and features, *J. Geophys. Res.*, *107*(E8), 5061, doi:10.1029/2001JE001584.

Basilevsky, A. T., and J. W. Head (2002b), On rates and styles of late volcanism and rifting on Venus, *J. Geophys. Res.*, *107*(E6), 5041, doi:10.1029/2000JE001471.

Basilevsky, A. T., and J. W. Head (2006), Impact craters on regional plains on Venus: Age relations with wrinkle ridges and implications for the geological evolution of Venus, *J. Geophys. Res.*, *111*, E03006, doi:10.1029/2005JE002473.

Basilevsky, A. T., R. O. Kuzmin, O. V. Nikolaeva, A. A. Pronin, L. B. Ronka, V. S. Avduevsky, G. R. Uspensky, Z. P. Cheremukhina, V. V. Semenchenko, and V. M. Ladygin (1985), The surface of Venus as revealed by the Venera landings: Part II, *Geol. Soc. Am. Bull.*, *96*, 137–144, doi:10.1130/0016-7606(1985)96<137:TSOVAR>2.0.CO;2.

Basilevsky, A. T., J. W. Head, and I. V. Setyaeva (2003), Venus: Estimation of age of impact craters on the basis of degree of preservation of associated radar-dark deposits, *Geophys. Res. Lett.*, *30*(18), 1950, doi:10.1029/2003GL017504.

Basilevsky, A. T., J. W. Head, and A. M. Abdrakhimov (2004), Impact crater air fall deposits on the surface of Venus: Areal distribution, estimated thickness, recognition in surface panoramas, and implications for provenance of sampled surface materials, *J. Geophys. Res.*, *109*, E12003, doi:10.1029/2004JE002307.

Bondarenko, N. B., and J. W. Head (2004), Radar-dark impact crater-related parabolas on Venus: Characterization of deposits with Magellan emissivity data, *J. Geophys. Res.*, *109*, E09004, doi:10.1029/2004JE002256.

Bondarenko, N. V., M. A. Kreslavsky, and J. W. Head (2006), North-south roughness anisotropy on Venus from the Magellan radar altimeter: Correlation with geology, *J. Geophys. Res.*, *111*, E06S12, doi:10.1029/2005JE002599.

Brackett, R. A., B. Fegley, and R. E. Arvidson (1995), Volatile transport on Venus and implications for surface geochemistry and geology, *J. Geophys. Res.*, *100*, 1553–1563, doi:10.1029/94JE02708.

Campbell, B. A. (1994), Merging Magellan emissivity and SAR data for analysis of Venus surface dielectric properties, *Icarus*, *112*, 187–203, doi:10.1006/icar.1994.1177.

Campbell, D. B., N. J. S. Stacy, W. I. Newman, R. E. Arvidson, E. M. Jones, G. S. Musser, A. Y. Roper, and C. Schaller (1992), Magellan observations of extended impact crater related features on the surface of Venus, *J. Geophys. Res.*, *97*, 16,249–16,277.

Campbell, M. J., and J. Ulrichs (1969), Electrical properties of rocks and their significance for lunar radar observations, *J. Geophys. Res.*, *74*, 5867–5881, doi:10.1029/JB074i025p05867.

Carrier, W. D., G. R. Olhoeft, and W. Mendell (1991), Physical properties of the lunar surface, in *Lunar Source- Book*, edited by G. Heiken, D. Vaniman, and B. French, pp. 475–594, Cambridge Univ. Press, New York.

Carter, L. M., D. B. Campbell, and B. A. Campbell (2004), Impact crater related surficial deposits on Venus: Multipolarization radar observations with Arecibo, *J. Geophys. Res.*, *109*, E06009, doi:10.1029/2003JE002227.

Fegley, B., M. Yu. Zolotov, and K. Lodders (1997), The oxidation state of the lower atmosphere and surface of Venus, *Icarus*, *125*, 416–439, doi:10.1006/icar.1996.5628.

Florensky, K. P., L. B. Ronka, A. T. Basilevsky, G. A. Burba, O. V. Nikolaeva, A. A. Pronin, A. M. Trakhtman, V. P. Volkov, and V. V. Zazetsky (1977), The surface of Venus as revealed by Soviet Venera 9 and 10, *Geol. Soc. Am. Bull.*, *88*, 1537–1545, doi:10.1130/0016-7606(1977)88<1537:TSOVAR>2.0.CO;2.

Ford, P. G., and G. H. Pettengill (1992), Venus topography and kilometer-scale slopes, *J. Geophys. Res.*, *97*, 13,103–13,114.

Garvin, J. B. (1990), The global budget of impact-derived sediments on Venus, *Earth Moon Planets*, *50–51*, 175–190, doi:10.1007/BF00142394.

Garvin, J. B., J. W. Head, M. T. Zuber, and P. Helfenstein (1984), Venus: The nature of the surface from Venera panoramas, *J. Geophys. Res.*, *89*, 3381–3399, doi:10.1029/JB089iB05p03381.

Garvin, J. B., J. W. Head, G. H. Pettengill, and S. H. Zisk (1985), Venus global radar reflectivity and correlation with elevation, *J. Geophys. Res.*, *90*, 6859–6871, doi:10.1029/JB090iB08p06859.

Greeley, R., K. Bender, P. E. Thomas, G. Schubert, D. Limonadi, and C. M. Weitz (1995), Wind-related features and processes on Venus: Summary of Magellan results, *Icarus*, *115*, 399–420, doi:10.1006/icar.1995.1107.

Greeley, R., K. C. Bender, R. S. Saunders, G. Schubert, and C. M. Weitz (1997), Aeolian processes and features on Venus, in *Venus II: Geology, Geophysics, Atmosphere, and Solar Wind Environment*, edited by S. W. Bougher, D. M. Hunten, and R. J. Philips, pp. 547–590, Univ. of Ariz. Press, Tucson.

Head, J. W., and L. Wilson (1992), Magma reservoirs and neutral buoyancy zones on Venus: Implications for the formation and evolution of volcanic landforms, *J. Geophys. Res.*, *97*, 3877–3903.

Herrick, R. R., and R. J. Phillips (1994), Implications of a global survey of Venusian impact craters, *Icarus*, *111*, 387–416, doi:10.1006/icar.1994.1152.

Herrick, R. R., V. L. Sharpton, M. C. Malin, S. C. Lyons, and K. Feely (1997), Morphology and morphometry of impact craters, in *Venus II: Geology, Geophysics, Atmosphere, and Solar Wind Environment*, edited by S. W. Bougher, D. M. Hunten, and R. J. Phillips, pp. 1015–1046, Univ. of Ariz. Press, Tucson.

Izenberg, N. R., R. E. Arvidson, and R. J. Phillips (1994), Impact crater degradation on Venusian plains, *Geophys. Res. Lett.*, *21*, 289–292, doi:10.1029/94GL00080.

Keddie, S. T., and J. W. Head (1995), Formation and evolution of volcanic edifices on the Dione Regio rise, Venus, *J. Geophys. Res.*, *100*, 11,729–11,754, doi:10.1029/95JE00822.

Kemurdzhian, A. L., P. N. Brodskii, V. V. Gromov, V. P. Grushin, I. E. Kiselev, G. V. Kozlov, A. V. Mitskevich, V. G. Perminov, P. S. Sologub, and A. D. Stepanov (1983), Preliminary results of determining the physical and mechanical properties of the soil of Venus by Soviet automatic stations Venera 13 and Venera 14, (in Russian), *Kosm. Issled.*, *21*, 323–330.

Kreslavsky, M. A., and R. V. Vdovichenko (1999), Anisotropy of Venus surface properties inferred from Magellan side-looking-radar data, *Sol. Syst. Res., Engl. Transl.*, *33*, 110–119.

Marshall, J. R., G. Fogleman, R. Greeley, R. Hixon, and D. Tucker (1991), Adhesion and abrasion of surface materials in the Venusian aeolian environment, *J. Geophys. Res.*, *96*, 1931–1947, doi:10.1029/90JB00790.

Muhleman, D. O. (1964), Radar scattering from Venus and the Moon, *Astron. J.*, *69*, 34–41, doi:10.1086/109225.

Pettengill, G. H., P. G. Ford, and B. G. Chapman (1988), Venus: Surface electromagnetic properties, *J. Geophys. Res.*, *93*, 14,881–14,892, doi:10.1029/JB093iB12p14881.

Pettengill, G. H., P. G. Ford, and R. G. Wilt (1992), Venus surface radiothermal emission as observed by Magellan, *J. Geophys. Res.*, *97*, 13,091–13,103.

Phillips, R. J., R. F. Raubertas, R. E. Arvidson, I. C. Sarkar, R. R. Herrick, N. Izenberg, and R. E. Grimm (1992), Impact craters and Venus resurfacing history, *J. Geophys. Res.*, *97*, 15,923–15,948.

Schaller, C. J., and H. J. Melosh (1998), Venusian ejecta parabolas: Comparing theory with observations, *Icarus*, *131*, 123–137, doi:10.1006/icar.1997.5855.

Schultz, P. H. (1992), Atmospheric effects on ejecta emplacement, *J. Geophys. Res.*, *97*, 11,623–11,662.

Shaber, G. G., R. G. Strom, H. J. Moore, L. A. Soderblom, R. L. Kirk, D. J. Chadwick, D. D. Dawson, L. R. Gaddis, J. M. Boyce, and J. Russel (1992), Geology and impact craters on Venus: What are they telling us?, *J. Geophys. Res.*, *97*, 13,257–13,301.

Shepard, M. K., B. A. Campbell, M. H. Bulmer, T. G. Farr, L. R. Gaddis, and J. J. Plaut (2001), The roughness of natural terrain: A planetary and remote sensing perspective, *J. Geophys. Res.*, *106*, 32,777–32,795, doi:10.1029/2000JE001429.

Stratton, J. A. (1947), *Electromagnetic Theory*, 615 pp., John Wiley, New York.

Tyler, G. L., R. A. Simpson, M. J. Maurer, and E. Holmann (1992), Scattering properties of the Venusian surface: Preliminary results from Magellan, *J. Geophys. Res.*, *97*, 13,115–13,139.

Ulaby, F. T., R. K. Moore, and A. K. Fung (1986), *Microwave Remote Sensing: Active and Passive*, Artech House, Norwell, Mass.

Vervack, R. J., Jr., and H. J. Melosh (1992), Wind interaction with falling ejecta: Origin of the parabolic features on Venus, *Geophys. Res. Lett.*, *19*, 525–528, doi:10.1029/91GL02812.

Weitz, C. M., and A. T. Basilevsky (1993), Magellan observations of the Venera and Vega landing site regions, *J. Geophys. Res.*, *98*, 17,069–17,098, doi:10.1029/93JE01776.

Weitz, C. M., J. J. Plaut, R. Greeley, and R. S. Saunders (1994), Dunes and microdunes on Venus: Why were so few found in the Magellan data?, *Icarus*, *112*, 282–295, doi:10.1006/icar.1994.1181.

Williams, S. H., and R. Greeley (1994), Windblown sand on Venus: The effect of high atmospheric density, *Geophys. Res. Lett.*, *21*, 2825–2828, doi:10.1029/94GL02762.

Wood, J. A. (1997), Rock weathering on the surface of Venus, in *Venus II: Geology, Geophysics, Atmosphere, and Solar Wind Environment*, edited by S. W. Bougher, D. M. Hunten, and R. J. Phillips, pp. 637–664, Univ. of Ariz. Press, Tucson.

N. V. Bondarenko and J. W. Head, Department of Geological Sciences, Brown University, Providence, RI 02912, USA. (natasha@mare.geo.brown.edu)